Sheffield Hallam University | Department of Engineering & Mathematics

FORMULA STUDENT SHURACING

William W. Hodgett
b8005109
MEng (Hons) Aerospace Engineering

A Study into How Varying Yaw Angles Affect the Aerodynamic Performance of a Formula Student Front Wing

Dissertation submitted in partial fulfilment of the requirements of the degree of Bachelor of Science

Preface

This report describes project work carried out within the Department of Engineering & Mathematics at Sheffield Hallam University between October 2022 and April 2023, exploring the changes in aerodynamic performance on a Formula Student front wing, when introduced to variations in yaw.

The submission of the report is in accordance with the requirements for the award of the degree of Bachelor of Engineering in Aerospace Engineering under the auspices of the University.

Acknowledgements

I would like to take the opportunity to express my appreciation to Dr Harish Viswanathan for his continued support and guidance throughout this project. Additionally, I would like to thank Findley Scrivner and the management of the SHU Racing team for their assistance and advice throughout, as well as Simon Apps for taking an interest and aiding in operation of the wind-tunnel.

Abstract.

This report provides the outline of the analysis of a Formula Student front wing at varying degrees of yaw, carried out in collaboration with the Sheffield Hallam University Racing Team, with the intention of understanding the effects cornering has on the aerodynamic performance of the vehicle, to drive future improvement. Where optimal improvement to cornering performance was observed to occur with enhancement of the aerodynamic performance.

Where computational limits have restricted the analysis to a single component, the front wing was considered the most vital due to its importance in conditioning the airflow over the remainder of the vehicle, as it is the first component to encounter undisturbed air.

CFD simulations for varying degrees of yaw between 0° - 8° at variations of 2°, using the realizable k-epsilon turbulence model with an enhanced wall treatment, have been carried out, as well as comparisons being made against the k-omega SST turbulence model, experimental data, and the same geometry outside of ground proximity.

Findings from the observation saw a gradually decreasing slope for lift as well as an almost linearly decreasing drag force and almost linearly increasing side force, with increasing yaw angle. The focus for alterations to the geometry were based around the vortex generation in the wake region below the element cascades, as well as the increased airflow against the side plates, as these areas showed the most variation with increasing yaw angle.

Further improvement has been made to the geometry through the addition of a flat footplate, which delays the onset of mixing between the high- and low-pressure regions below and outside the wing, where a ~12% increase across yaw angles and 13.59% increase at 0° yaw, in downforce was seen with minimal increase in drag.

Contents

Table of Figures

Table of Tables

1. Introduction

1.1. Formula Student

Each year IMechE Formula Student runs an event where students from various universities around the world, have the opportunity to demonstrate engineering skills and understanding, through the design and manufacturing of a Formula Student vehicle, which is used to compete in static and dynamic events within a competitive motorsport environment, thus giving students the chance to demonstrate, develop and improve upon skills which can be used within industry.

The Formula Student challenge consists of the production of a single seat race car for the purpose of sprint or autocross racing, which is then presented to a hypothetical manufacturing firm. Aspects that require consideration for production include cost, maintenance, reliability, performance, and handling. Logic behind design decisions need to be justified with an additional requirement of viability for both parties.

Testing within the event consists of two main phases made up of static and dynamic events.

Static Events:

- Design, cost, sustainability, and business presentation judging.
- Technical and safety scrutineering
- Tilt test
- Brake and noise test

Dynamic Events:

- Skid pad
- Sprint
- Acceleration
- Endurance
- Fuel economy

(IMechE. 2023)

The dynamic events are where efforts made in prototyping and manufacturing are put to the test, therefore having an understanding of how the vehicle is going to perform under event conditions is beneficial.

The development of aerodynamic components on a formula student vehicle provides a competitive edge when competing in the dynamic events, as most of these events consist of short layouts with tight corners, thus the inclusion of an aerodynamic package provides an increase in downforce with a reduction in drag, permitting the vehicle to accelerate to greater speeds within a shorter period of time.

1.2. Sheffield Hallam University Racing

SHU Racing is the Sheffield Hallam University Formula Student team, where each year SHU students from a diverse range of courses and backgrounds, with varying levels of experience, collaborate by combining strengths and skill-sets to design and manufacture a single seat race car, which is used to compete in the IMechE Formula Student event held in Silverstone.

Development is a major factor within the SHU Racing team, with additions and improvements being made each year, to further push the competitive edge of the vehicle during the event. Progression of the aerodynamic package currently implemented onto the vehicle is relatively new, with 2019 being the first year where the vehicle has run an aerodynamic package at the event, therefore making this an area of interest for continuous improvement.

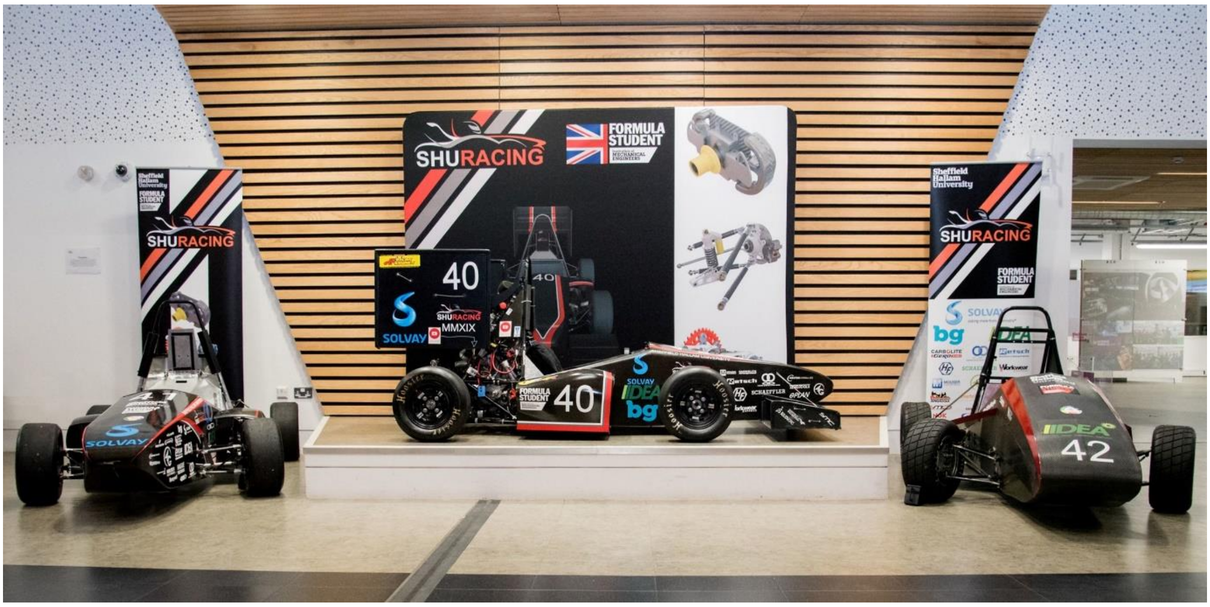

Figure 1-1: Previous SHU Racing Vehicles (SHU Racing Team)

1.3. Motorsport Frontwing Aerodynamics

The front wing may be considered as one of the most important aerodynamic components on a race car, as it is the first component that encounters undisturbed air, therefore conditioning the airflow over the remainder of the vehicle.

The front wing is essentially made up of a series of inverted aerofoils with varying chord lengths positioned at increasing angles of attack, where an aerofoil produces lift under Bernoulli’s principle, where air flowing over the upper surface of the aerofoil, flows at a higher velocity, creating an area of low pressure, while air flowing over the lower surface of the aerofoil flows at a lower velocity, creating an area high pressure, the pressure difference between the upper and lower surfaces then generates a lift force, which in the case of an inverted aerofoil would be considered as downforce.

One aspect of the front wing which increases its effectiveness in producing downforce is the presence of the ground effect. Due to the front wing operating within close proximity to the ground, a venturi effect is apparent where a convergent divergent section is created between the lower surface of the aerofoil and the ground, thus accelerating the flow underneath the lower element, in accordance with Bernoulli’s principle. With an increase in flow velocity under the element comes the effect of further decreasing the low-pressure region created by the aerofoil, this then creates a greater pressure difference between the upper and lower surface of the aerofoil, thus increasing the lift force generated without the effects of increased drag which become apparent with increasing angle of attack.

Taking into account the fact that the front wing is such a crucial component in improving the performance of the vehicle, it is therefore highly beneficial to have an understanding of how this component performs under event conditions. Many teams achieve this through the use of CFD simulation, however due to the high computational costs and timescales required, performance is usually only analysed with the vehicle traveling in a straight line at a 0° yaw angle, with results being used to optimise the package under these conditions. The dynamic events included in Formula Student however, involve short, tight tracks with numerous corners, chicanes and curves meaning the vehicle very rarely travels in a straight line across the event, therefore analysis of the vehicle without cornering, does not give an accurate representation of how the vehicle is likely to perform across the whole event.

This report is therefore intended to increase the understanding of the aerodynamic performance of the SHU Racing vehicle under cornering conditions through CFD analysis, where findings are to be used in future development of the vehicle, however due to the limitations of computational resources available at present, the analysis has been limited to the front wing due to its importance.

Figure 1-2: 2022 SHU Racing Vehicle (SHU Racing Team)

1.4. Cornering Conditions

Taking into account the forces acting on the vehicle in cornering conditions, it can be seen through the derivation in equation-(1) that the maximum tangential velocity the vehicle can achieve while traveling around a corner is dependent on the friction forces between the tyres and the ground, where the friction forces prevent the vehicle from going into a slide. Therefore, in order to increase the velocity of the cornering vehicle, the friction force needs to be increased, this can be achieved through increasing the downforce created by the aerodynamic components, without the negative effects that come with increasing weight.

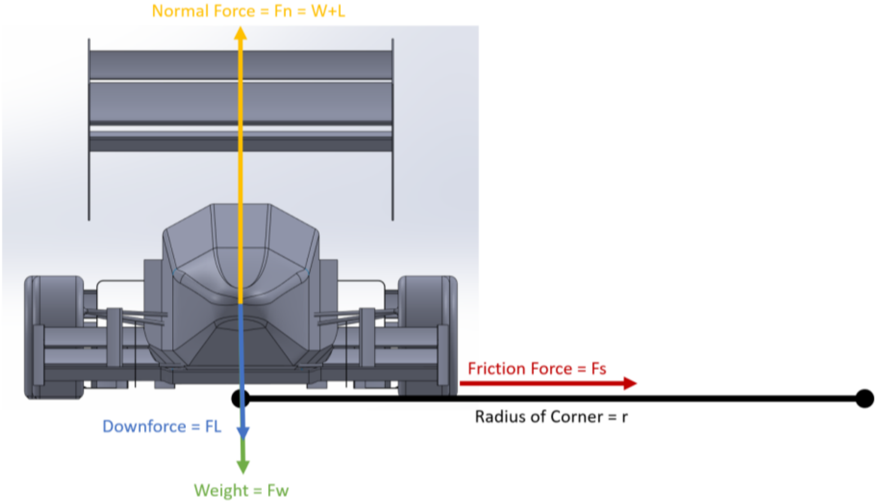

Figure 1-3: Forces Acting on the Vehicle Front-on

$$F_{Net} = ma$$

$$\mu_{F_s} \times F_n = m\frac{V^2}{r}$$

$$\mu_{F_s}(F_W + F_L) = m\frac{V^2}{r} \qquad \ldots (1)$$

$$V_{max} = \sqrt{\frac{\mu_{F_s}(F_W + F_L)r}{m}}$$

While in figure-1-4 it can be seen that in order to achieve forward motion the engine has to overcome the friction forces generated by the tyres and drag imposed on the vehicle, therefore a balance between drag reduction and downforce needs to be considered when designing aerodynamic components, thus further creating the need for an understanding of how the vehicle performs under cornering conditions.

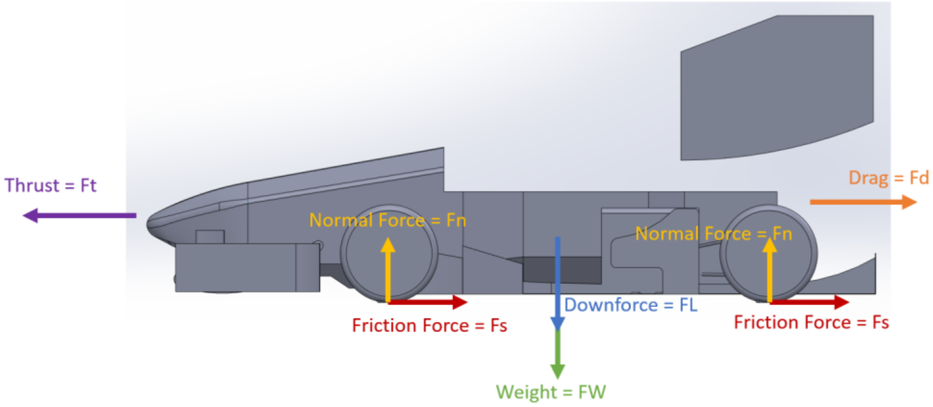

Figure 1-4: Forces Acting on the Vehicle Side-on

2. Literature Review

An entry by Agathangelou et al. (1998) shows the difference in lap times for a 10% increase in downforce or 10% decrease in drag, where a ~0.7s reduction in lap time is seen, and a 10% increase in tyre grip resulted in a ~3s reduction in lap time. As differences in positions in motorsport competitions are usually based around tenths of seconds, this reduction in lap time built up over the course of the race can have a major effect on the competing teams' position, thus showing that even a small improvement in aerodynamic performance can create a competitive edge. The entry also claims that the front wing is responsible for around 25%-30% of the downforce produced by the vehicle, outlining the importance of the front wing in terms of vehicle performance, thus further justifying the component choice for analysis.

A study completed by Roberts et al. (2016) on Aerodynamic characteristics of a wing & flap configuration in ground effect & yaw, published to show the fundamental effects of yaw on a simplified front wing, where analysis performed by motorsport teams are rarely published due to competitive secrecy, suggests that during cornering, two yaw effects are generated, constant yaw angle due to side slip as well as dynamic yaw rate, suggesting the vehicle will experience changing yaw angles during the cornering manoeuvre. It is also suggested that the yaw rate can be quite high, up to 50°/sec, but is only significant during events such as the initial turn into the corner, the yaw angle is however, felt throughout the corner and is predicted to be around 3°-5°.

Additionally, although the yaw angle changes throughout the corner, yaw rate is not high enough, other than the initial turn in event, to warrant using anything other than quasi static analysis. Where the difference in flow angle between the leading and trailing edges is observed to be small.

This approach is to be adopted for this report where an analysis for the front wing at various fixed degrees of yaw is to take place, with yaw angles ranging from 0°-8°, thus encompassing the 3°-5° predicted, with additional variance on either side, changes in yaw angle are to be limited to 2° as to reduce the computational cost of the analysis.

Findings from the report by Roberts et al. (2016) also focus on the difference in vortex generation on either side of the wing due to variations in yaw, as well as the change in pressure distribution across the wing. Taking this into account these factors are to be observed when analysing the flow structure across the wing. Findings from the report observe diminishing downforce and drag for increasing yaw angle.

A paper by Patel et al. (2021) also compares lift, drag and side forces under fixed yaw and cornering compared to straight-line operating conditions, where minimal variation is observed between cornering and fixed yaw conditions, also concluding that "representative data for forces experienced during the corner can be obtained from a fixed yaw test for an isolated wing." Further justifying the analysis being performed for varying degrees of fixed yaw.

A study by H. Viswanathan (2021) investigates the Aerodynamic performance of several passive vortex generator configurations on an Ahmed body subjected to yaw angles, shows that trapezoidal vortex generators can be used to produce favourable aerodynamic performance improvements for yaw angles greater than 2°, as well as delta vortex generators producing favourable characteristics for yaw angles less than 4°. If separation is observed on the wing vortex generators could be easily integrated into the design to improve the flow characteristics where favourable alterations to the wake structure were seen through the implementation of various vortex generator types.

A study conducted by Guerrero et al. (2022) on the effect of rear underbody diffusers on road cars, states that aerodynamic drag is responsible for more than 50% of the propulsive fuel consumption of a typical car running on a highway, where a reduction in aerodynamic drag is more economical compared to improvements to other vehicle mechanisms. Where one of the main aims is to improve the performance of the vehicle to gain a competitive edge, events such as the endurance event award points for the fuel economy of the teams' vehicle where points are calculated based on the amount of fuel remaining in the vehicle by the end of the event. Thus, further improvement should take into account the fuel economy aspects, where design changes should consider either an increase in downforce with minimal to no increase in drag, or changes that result in a drag reduction.

The study also considers the airflow around the wheels as they have the effect of interfering with the airflow into the diffuser section, where vortices created by the wheelhouses have a significant effect on the aerodynamic loads of the vehicle and specific diffuser combinations may create the possibility of reaching minimal drag. As the front wing has the effect of conditioning the flow for the remainder of the vehicle, having an understanding of how this component performs in yaw could aid in designing components such as the diffuser where components acting within its proximity have an effect on its efficiency and performance.

A study by Martins et al. (2021) on the influence of front wing pressure distribution on wheel wake aerodynamics of a F1 car, concludes that vortex breakdown underneath the wing is one of the main downforce limiting factors and has considerable repercussions on its performance. Where vortex generation created by the front wing has an effect on the wake structure on the wake effects created by the front wheels. With this in mind, understanding how the vortex generation of the front wing is affected by variations in the yaw angle, could aid in a redesign where control the wake effects of the tyres could aid in enhancing the performance of components such as the diffuser, which are affected by the tyres.

A study by Read et al (2020) states that where the k-epsilon model has been successful in describing the aerodynamic properties on commercial vehicles and serves as a popular choice in industrial flows, the realizable k-epsilon turbulence model is based on the approach for which eddy viscosity is computed. With this factor in mind the realizable k-epsilon model is considered for use within this study. Where the study focused on the effects incline had on the vehicle side-wall interaction, an increase in side-wall incline saw an improvement in vehicle aerodynamic performance, these effects could be considered in endplate designs, where the current endplates are vertical, an incline could be introduced as a possible method to improve aerodynamic performance.

Katz, J. (2016). Describes the ground effect imposed on a vehicle in proximity to the ground, where flow over a body changes when it comes into proximity to a boundary, where vehicle streamlines close to the ground eventually become parallel to the ground. Both lift and drag increase as ground clearance is reduced however at low ground clearances stall occurs due to the reduced flow. As the front wing operates within ground proximity, to increase its effectiveness, this will be preserved during the analysis in order to maintain corelation with the relative scenario.

Katz, J. (2016). Also goes on to describe the benefits of increasing downforce has on tyre preservation, where increasing the normal force due to an increase in aerodynamic loads helps reduce heating and wear due to slip friction, thus increasing the life longevity of the vehicle components. The prevention of slip also increases vehicle stability where an increase in aerodynamic loads at the front or rear of the vehicle can prevent under or over steer as the vehicle goes into a corner, thus aerodynamic performance can be seen as a vital observation in cornering conditions to improve the stability of the vehicle.

3. Computational Fluid Dynamics Theory

3.1. Background

Computational fluid dynamics (CFD) can be described as the study of fluid flow through numerical simulation, where the basis is set around solving the governing equations of fluid dynamics which represent the conservation laws of physics.

The laws of physics involved include:

- The conservation of mass for the fluid
- Newton's second law
- The first law of thermodynamics

(Tu, Liu & Yeoh, 2018)

3.2. Governing Equations

3.2.1. Continuity Equation

The conservation of mass states that mass in an isolated system may neither be created nor destroyed, therefore fluid moving through a fixed control volume, fixed in space and time, across a control surface, requires that the change in mass within the control volume is equal to the mass flux over the control surface.

Where the mass conservation can be expressed as equation-(2)

$$\frac{\partial \rho}{\partial t} + \nabla \cdot (\rho V) = 0 \quad \dots (2)$$

Which can be expressed in terms of the cartesian coordinate system in equation-(3)

$$\frac{\partial \rho}{\partial t} + \frac{\partial (\rho u)}{\partial x} + \frac{\partial (\rho v)}{\partial y} + \frac{\partial (\rho w)}{\partial z} = 0 \quad \dots (3)$$

(Tu, Liu & Yeoh, 2018)

3.2.2. Momentum Equation

Newtons second law states that the sum of the forces acting on a fluid element are equal to the mass multiplied by the acceleration of that element, this can be expressed in equation-(4)

$$\Sigma F = ma \quad \dots (4)$$

This can further be split into components of the cartesian coordinate system, with equation-(5) shown in the x-direction.

$$\Sigma F_x = m_x a_x \quad \dots (5)$$

Where acceleration and mass of the fluid element can be expressed as equation-(6) & equation-(7).

$$a_x = \frac{Du}{Dt} \quad \dots (6)$$

$$m_x = \rho \Delta x \Delta y \Delta z \quad \dots (7)$$

Equation-(5) can then be described as equation-(8)

$$\Sigma F_x = \rho \frac{Du}{Dt} \Delta x \Delta y \Delta z \quad \dots (8)$$

Introducing the surface forces acting on the fluid element, made up of normal stresses σ and tangential stresses τ, the momentum equations in the x, y & z directions can then be defined as equation-(9), (10) & (11)

$$\rho \frac{Du}{Dt} = \frac{\partial \sigma_{xx}}{\partial_x} + \frac{\partial \tau_{yx}}{\partial_y} + \frac{\partial \tau_{zx}}{\partial_z} + \Sigma F_x^{body\ forces} \quad \dots (9)$$

$$\rho \frac{Dv}{Dt} = \frac{\partial \tau_{xy}}{\partial_x} + \frac{\partial \sigma_{yy}}{\partial_y} + \frac{\partial \tau_{zy}}{\partial_z} + \Sigma F_y^{body\ forces} \quad \dots (10)$$

$$\rho \frac{Dw}{Dt} = \frac{\partial \tau_{xz}}{\partial_x} + \frac{\partial \tau_{yz}}{\partial_y} + \frac{\partial \sigma_{zz}}{\partial_z} + \Sigma F_z^{body\ forces} \quad \dots (11)$$

(Tu, Liu & Yeoh, 2018)

3.2.3. Energy Equation

The conservation of energy can be defined as the change in internal energy of a system, is equal to the sum of the energy supplied due to heat addition and work done to the system.

Where the time rate of change of energy can be interpreted as equation-(12)

$$Time\ rate\ of\ change\ of\ energy = \rho \frac{DE}{Dt} \Delta x \Delta y \Delta z \quad \dots (12)$$

Accounting for the surface forces acting in the x, y & z directions, made up of the normal viscous stress σ and tangential viscous stress τ, equation-(12) can then be expressed as equation-(13).

$$\rho \frac{DE}{Dt} = \frac{\partial(u\sigma_{xx})}{\partial_x} + \frac{\partial(v\sigma_{yy})}{\partial y} + \frac{\partial(w\sigma_{zz})}{\partial_z} + \frac{\partial(u\tau_{yx})}{\partial y} + \frac{\partial(u\tau_{zx})}{\partial z} + \frac{\partial(v\tau_{xy})}{\partial x} + \frac{\partial(v\tau_{zy})}{\partial z} + \frac{\partial(v\tau_{xz})}{\partial x} + \frac{\partial(v\tau_{yz})}{\partial y} - \frac{\partial q_x}{\partial_x} - \frac{\partial q_y}{\partial_y} - \frac{\partial q_z}{\partial_z} \quad \dots (13)$$

(Tu, Liu & Yeoh, 2018)

3.3. Turbulence Models

3.3.1. RANS Equations

The conservation equations discussed previously may be used in relatively simple cases such as those involving laminar flow, however in more complex scenarios such as those where the effects of turbulence are present, further terms are required to accurately capture the turbulent flow regime.

Due to the chaotic nature of turbulence flow, properties need to be calculated using a time averaged approach, in order for this to be achieved the Reynolds-averaged Navier Stokes (RANS) equations are used, presented in equation-(14), (15) & (16)

Where the terms $\bar{u}, \bar{v}, \bar{p}$ represent mean values, u', v', p' represent turbulent fluctuations and $\overline{a'b'}$ represent the Reynolds stresses.

$$\frac{\partial \rho}{\partial t} + \frac{\partial(\rho\bar{u})}{\partial x} + \frac{\partial(\rho\bar{v})}{\partial y} = 0 \qquad \ldots (14)$$

$$\frac{\partial(\rho\bar{u})}{\partial t} + \frac{\partial(\rho\bar{u}\bar{u})}{\partial x} + \frac{\partial(\rho\bar{v}\bar{u})}{\partial y} = \frac{\partial\bar{p}}{\partial x} + \frac{\partial}{\partial x}\left(\mu\frac{\partial\bar{u}}{\partial x}\right) + \frac{\partial}{\partial y}\left(\mu\frac{\partial\bar{u}}{\partial y}\right) + \frac{\partial}{\partial x}\left[\mu\frac{\partial\bar{u}}{\partial x}\right] + \frac{\partial}{\partial y}\left[\mu\frac{\partial\bar{v}}{\partial x}\right] - \left[\frac{\partial(\rho\overline{u'u'})}{\partial x} + \frac{\partial(\rho\overline{u'v'})}{\partial y}\right] \qquad \ldots (15)$$

$$\frac{\partial(\rho\bar{v})}{\partial t} + \frac{\partial(\rho\bar{u}\bar{v})}{\partial x} + \frac{\partial(\rho\bar{v}\bar{v})}{\partial y} = \frac{\partial\bar{p}}{\partial y} + \frac{\partial}{\partial x}\left(\mu\frac{\partial\bar{v}}{\partial x}\right) + \frac{\partial}{\partial y}\left(\mu\frac{\partial\bar{v}}{\partial y}\right) + \frac{\partial}{\partial x}\left[\mu\frac{\partial\bar{u}}{\partial y}\right] + \frac{\partial}{\partial y}\left[\mu\frac{\partial\bar{v}}{\partial y}\right] - \left[\frac{\partial(\rho\overline{u'v'})}{\partial x} + \frac{\partial(\rho\overline{v'v'})}{\partial y}\right] \qquad \ldots (16)$$

The Boussinesq (1868) approach suggests the Reynolds stresses could be linked to mean rates of deformation, represented in equation-(17)

Where the term μ_T represents turbulent viscosity and k represents turbulent kinetic energy.

$$-\rho\overline{u'u'} = 2\mu_T\frac{\partial\bar{u}}{\partial x} - \frac{2}{3}\rho k; \quad -\rho\overline{v'v'} = 2\mu_T\frac{\partial\bar{v}}{\partial y} - \frac{2}{3}\rho k; \quad -\rho\overline{u'v'} = \mu_T\left(\frac{\partial\bar{v}}{\partial x} + \frac{\partial\bar{u}}{\partial y}\right) \qquad \ldots (17)$$

(Tu, Liu & Yeoh, 2018)

3.3.2. K-epsilon

The k-epsilon model consists of a two-equation model where two separate transport equations allow for turbulent velocity and length scales to be independently determined, this model has shown robustness, economy, and reasonable accuracy in predicting turbulent flows and is a popular option within industry. (Ansys, Inc. 2009)

In order to formulate the k-epsilon model the turbulent kinetic energy k and rate of dissipation of turbulent energy ε can be defined in cartesian tensor notation as equations-(18) & (19)

Where $i, j = 1,2,3$

$$k = \frac{1}{2} u_i' u_i' \qquad \dots (18)$$

$$\varepsilon = \nu_T \overline{\left(\frac{\partial u_i'}{\partial x_j}\right)\left(\frac{\partial u_i'}{\partial x_j}\right)} \qquad \dots (19)$$

Local turbulent viscosity μ_T equation-(20) formulated from local values for k and ε.

$$\mu_T = \rho C_\mu \frac{k^2}{\varepsilon} \qquad \dots (20)$$

Where turbulent viscosity ν_T is given in equation-(21)

$$\nu_T = \frac{\mu_T}{\rho} \qquad \dots (21)$$

The standard $k{-}\varepsilon$ model uses additional transport equations to capture the diffusive nature of turbulent flow represented by equations-(22) & (23)

$$\frac{\partial(\rho k)}{\partial t} + \frac{\partial(\rho u k)}{\partial x} + \frac{\partial(\rho v k)}{\partial y} = \frac{\partial}{\partial x}\left(\frac{\mu_T}{\sigma_k}\frac{\partial k}{\partial x}\right) + \frac{\partial}{\partial y}\left(\frac{\mu_T}{\sigma_k}\frac{\partial k}{\partial y}\right) + P - D \qquad \dots (22)$$

$$\frac{\partial(\rho \varepsilon)}{\partial t} + \frac{\partial(\rho u \varepsilon)}{\partial x} + \frac{\partial(\rho v \varepsilon)}{\partial y} = \frac{\partial}{\partial x}\left(\frac{\mu_T}{\sigma_\varepsilon}\frac{\partial \varepsilon}{\partial x}\right) + \frac{\partial}{\partial y}\left(\frac{\mu_T}{\sigma_\varepsilon}\frac{\partial \varepsilon}{\partial y}\right) + \frac{\varepsilon}{k}(C_{\varepsilon 1} P - C_{\varepsilon 2} D) \qquad \dots (23)$$

Where the destruction term D is represented by $\rho\varepsilon$, and the production term P is represented by equation-(24)

$$p = 2\mu_T\left[\left(\frac{\partial u}{\partial x}\right)^2 + \left(\frac{\partial v}{\partial y}\right)^2\right] + \mu_T\left(\frac{\partial u}{\partial y} + \frac{\partial v}{\partial x}\right)^2 - \frac{2}{3}\mu_T\left(\frac{\partial u}{\partial_x} + \frac{\partial v}{\partial y}\right)^2 - \frac{2}{3}\rho\mu_T k\left(\frac{\partial u}{\partial x} + \frac{\partial v}{\partial y}\right) \qquad \dots (24)$$

(Tu, Liu & Yeoh, 2018)

An improved version of the standard k-epsilon model is the realizable model, which contains new formulations for the turbulent viscosity and a new transport equation for the dissipation rate ε and is likely to provide superior performance in terms of flows involving rotations, boundary layers under strong adverse pressure gradients, separation, and recirculation. Initial studies have also shown that the realizable model provides the best performance of all the k-epsilon models in terms of separated flow with complex secondary flow features. (Ansys, Inc. 2009)

Due to k-epsilon models downfall in resolving the near wall region, an enhanced wall treatment may be employed as a method to further extend the validity of near wall modelling.

3.3.3. K-omega

An alternative model to k-epsilon is the k-omega model, which incorporates modifications for low-Reynolds-number effects, compressibility and shear flow spreading and has been shown to have better applicability in terms of wall-bounded and free shear flows. The transport equations used to solve the k-omega model are based on turbulent kinetic energy k and specific dissipation rate w, essentially the ratio of $\varepsilon\ to\ k$.

The transport equations for turbulent kinetic energy k and specific dissipation rate w are represented by equations-(25) & (26)

$$\frac{\partial}{\partial t}(\rho k) + \frac{\partial}{\partial x_i}(\rho k u_i) = \frac{\partial}{\partial x_j}\left(\Gamma_k \frac{\partial k}{\partial x_j}\right) + G_k - Y_k + S_k \qquad \ldots (25)$$

$$\frac{\partial}{\partial_t}(\rho w) + \frac{\partial}{\partial x_i}(\rho w u_i) = \frac{\partial}{\partial x_j}\left(\Gamma_w \frac{\partial w}{\partial x_j}\right) + G_w - Y_w + S_w \qquad \ldots (26)$$

Where G_k represents the generation of turbulence kinetic energy due to mean velocity gradients, G_w represents the generation of w, Γ_k and Γ_w represent the effective diffusivity of k and w due to turbulence, and S_k and S_w are user defined source terms.

(Ansys, Inc. 2009)

An alternative version of the k-omega model called the k-omega shear stress transport (SST) model is used to combine the accuracy of the k-omega model within the near wall region with the free stream independence of the k-epsilon model. The SST model contains additional features such as a blending function which activates the k-omega model in the near wall region and the k-epsilon model further away from the surface, these additional features make the SST model more accurate and reliable for a wider class of flows than the standard model. (ANSY, Inc. 2009)

Both the k-epsilon-realizable and k-omega-SST models will be explored and compared within this study, however due to the higher computational cost of the k-omega SST model, the realizable k-epsilon model will be utilised as the primary turbulence model.

4. Meshing Practices

4.1. Element types

4.1.1. Tetrahedral Elements

In cases where geometry of high complexity is used, unstructured meshes are often generated using tetrahedral elements without the complexity and additional user input that structured meshes often require. In cases of structured meshing, often made up of hexahedral elements, cells can often become quite skewed as they are deformed in order to fit the cells to the shape of the geometry, this can lead to inaccuracies, these factors are avoided when using an unstructured mesh however, a greater number of elements are required to fill the bounding area as well as the arbitrary number of neighbouring cells leads to increased solve times and computational cost. (Tu, Liu & Yeoh, 2018)

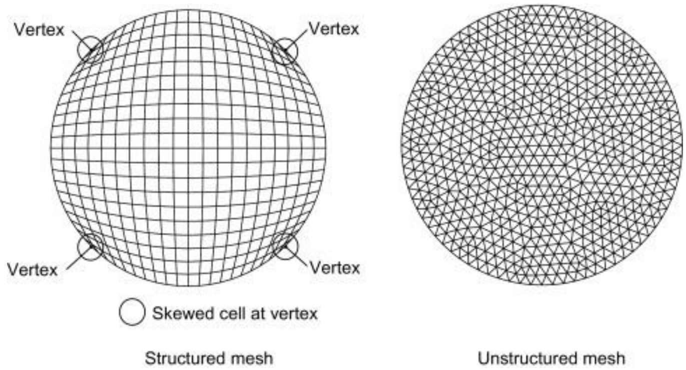

Figure 4-1: Structured vs Unstructured Mesh (Tu, Liu &Yeoh, 2018)

4.1.2. Poly-Hexcore Elements

A Mosaic meshing technology developed by Ansys Fluent allows the generation of meshes where multiple element types are combined using an automated meshing system. A Poly-Hexcore mesh is generated using octree hex elements in the bulk region, while maintaining a poly-prism boundary layer, these two mesh types are then connected using polyhedral elements. Where hex elements have shown a reduction in computing time and layered poly-prisms have shown increased accuracy in emulating the near wall boundary layer, while general poly elements provide a high-quality transition between mesh types. According to Ansys this meshing method has shown a 20-50% decrease in computational time when compared to similar meshing methods of the same accuracy.

With these desirable meshing aspects in mind, Poly-Hexcore meshing will be used for the completion of this report, in order to reduce the computational cost as much as possible.

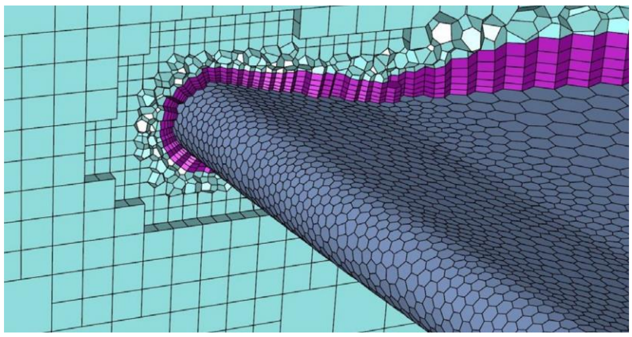

Figure 4-2: Poly-Hexcore Mesh Example (ANSYS)

4.2. Mesh Quality

4.2.1. Skewness

Skewness can be defined as the difference between the shape of a cell and shape of an equilateral cell of equivalent volume. Highly skewed cells can cause inaccuracies in results, ideal quadrilateral meshes have vertex angles close to 90°, while triangular meshes have angles close to 60° and all angles less than 90°, skewness ranges between values 0-1 with 1 being considered unacceptable and 0 being optimal.

Guidelines by Ansys suggest a maximum skewness of less than 0.95 with an average of less than 0.33, where greater values may lead to issues with convergence.

(Ansys, 2009)

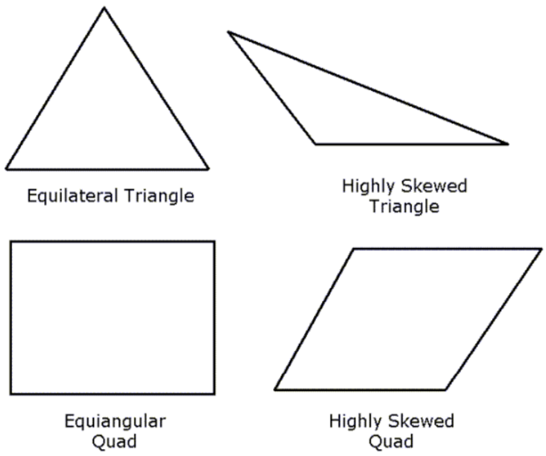

Figure 4-3: Skewness Example (Ansys, 2010)

4.2.2. Orthogonal Quality

The orthogonal quality for cells is computed using the face normal vector, the vector from the cell centroid to the centroid of each of the adjacent cells, and the vector from the cell centroid to each of the faces and is a measure of the overall shape of the cell.

Values for orthogonal quality lie within a range of 0-1 with 0 being considered unacceptable quality and 1 being considered optimal.

(Ansys, 2010)

4.2.3. Aspect Ratio

Aspect ratio can be defined as the measure of the stretching of a cell, where it is calculated by taking the ratio of the maximum value to minimum value of either of these distances:

- The distances between the cell centroid and face centroids
- The distances between the cell centroid and nodes.

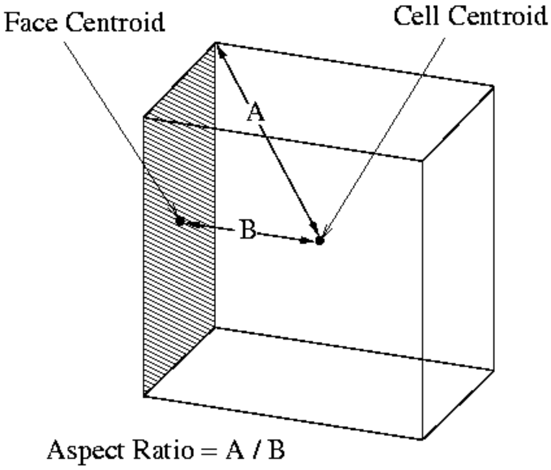

Figure 4-4: Aspect Ratio Diagram (Ansys, 2009)

Guidelines by Ansys suggest that aspect ratios greater than 5:1 should be avoided further away from the wall in the bulk flow, while cells within the boundary layer can be stretched to an aspect ratio of up to 10:1.

(Ansys, 2009)

4.3. Boundary Layer

In order to effectively capture and resolve the steep velocity gradient that occurs within the boundary layer when a viscous fluid flows over a surface, inflation layers are implemented as a means to efficiently generate a fine structured mesh extending from the surface to cover the boundary thickness without the need to refine the bulk mesh, which would result in a large increase in element count, therefore contributing to a reduction in computational cost.

The boundary layer thickness can be calculated as the distance from the wall up to the point where the near wall velocity reaches 99% of the free stream velocity, the Blasius solution can be used to approximate the thickness of the boundary layer $\delta 99$ for Re<5x10^5 equation-(27)

$$\delta_{99} = \frac{4.91 \times L}{\sqrt{Re_L}} \quad \dots (27)$$

Where the Reynolds number can be calculated using equation-(28)

$$Re = \frac{\rho V L}{\mu} \quad \dots (28)$$

In order to capture the effects of the viscous sub layer the inflation layer needs to be sufficiently refined closer to the wall where the dimensionless value for y+ is used in equation-(29) to estimate the first layer height, further changes within the CFD programme are required to sufficiently adjust the first layer height in order to achieve the desired y+ value.

$$y = \frac{y^{+}\mu}{\mu_{\tau}\rho} \qquad \ldots (29)$$

Where the skin friction coefficient is approximated using the Reynolds number in Prandtl's 1/7 power law show in equation-(30)

$$C_f = \frac{0.027}{Re^{1/7}} \qquad \ldots (30)$$

The wall shear stress is approximated using the skin friction coefficient in equation-(31)

$$\tau_w = \frac{1}{2} C_f \rho U_{\infty}^{2} \qquad \ldots (31)$$

And the friction velocity can be approximated using the wall shear stress in equation-(32)

$$\mu_{\tau} = \sqrt{\frac{\tau_w}{\rho}} \qquad \ldots (32)$$

For the k-omega model a y+≤1 is required to resolve the viscous sub layer, however for the realizable k-epsilon model where an enhanced wall treatment is employed, a y+~1 is recommended by Ansys to resolve the laminar sub-layer, however a y+ value residing well within the viscous sub-layer is still acceptable y+≤5.

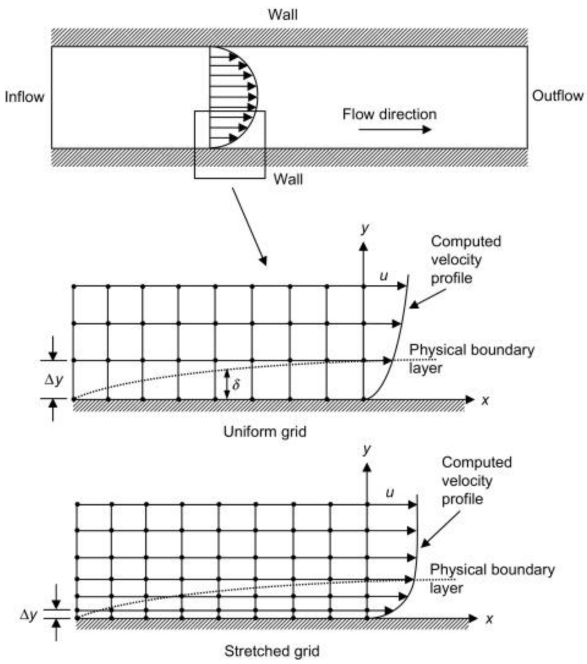

Figure 4-5: Boundary Layer Depiction (Tu, Liu &Yeoh, 2018)

5. Computational and Experimental Procedure

5.1. Computational Procedure

5.1.1. Geometry Setup

A CAD draft version of the SHU Racing front wing has been provided by the aerodynamics department. In order to reduce the computational cost of the simulation, an analysis is only being performed on the front wing without the inclusion of the vehicle body, in addition to this, complex features which have little effect on the aerodynamics of the model have been removed, examples of these include, small scale fixturing features (e.g., nuts, bolts, screws), the attachment arms between the wing and the body and any attachment holes, these changes should have little effect on the overall result and should provide an accurate approximation of the aerodynamic values within the simulation.

The overall design of the front wing consists of a multi-element wing, where the main element is positioned in the lower region with cascading elements consisting of increasing angles of attack on either side, the main element includes a stepped region in mid-section to increase the flow towards the undertray, tusks are positioned on the main element with the purpose of redirecting flow towards the outer edges of the wing, while curved side plates are positioned on either side of the wing to redirect flow away from the wheels, while reducing induced drag caused by vortices generated by the mixing of the high pressure and low pressure regions on either side of the elements, and wing fences are used as a structural component.

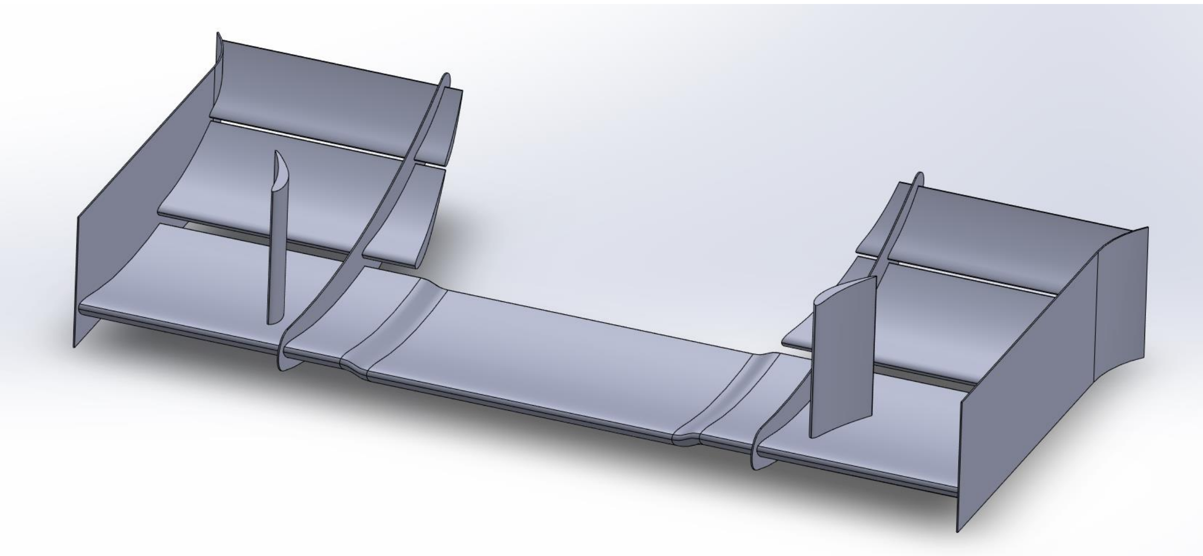

Figure 5-1: Front Wing Geometry

With the intentions of using wind tunnel testing as a validation method, the model has been scaled down to fit within the working section of the SHU wind tunnel, with scaling calculations being demonstrated in the following section, in addition to this the enclosure has been generated using the same dimensions as the working section of the SHU wind tunnel in order to approximate similar conditions, to further approximate wind tunnel conditions, the model has been positioned 1/3 of the length of the working section away from the enclosure inlet which is in correlation to the position within the wind tunnel.

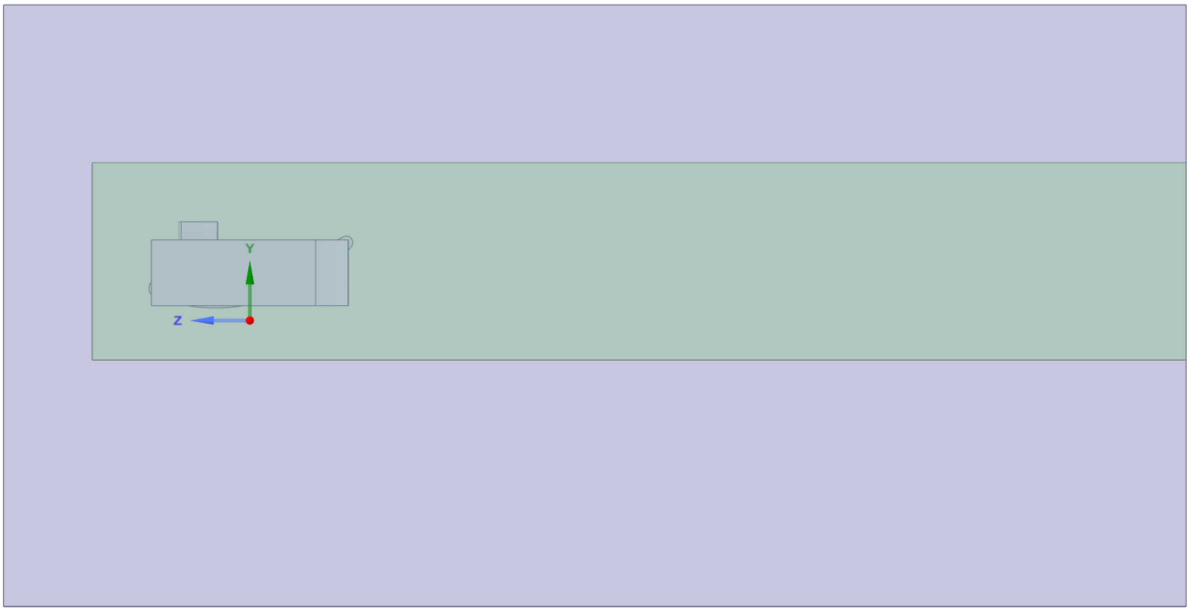

Figure 5-2: Enclosure

When generating the initial mesh, it was noticed that greater refinement was required around the leading and trailing edges of the aerofoils, in order to reduce the cell-count, a split was created in these regions, allowing for named selections to be created as well as enabling local mesh refinement, shown in figure-5-3.

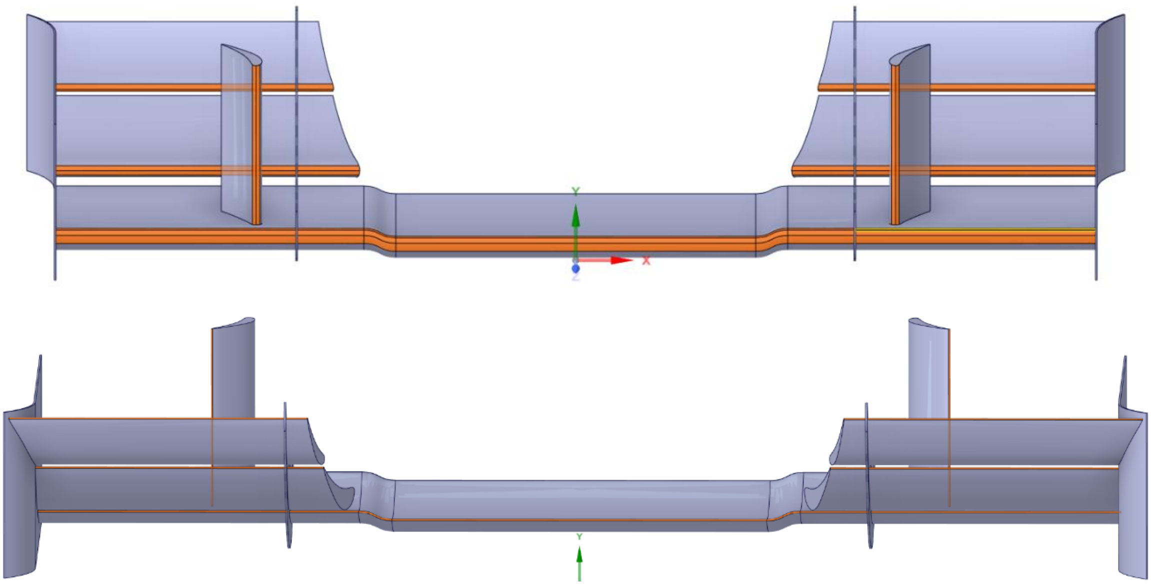

Figure 5-3: Leading & Trailing Edges Named Selections

The trailing edges of the aerofoils consist of radial edges due to manufacturing limitations, where the actual aerofoils would come to a point in reality.

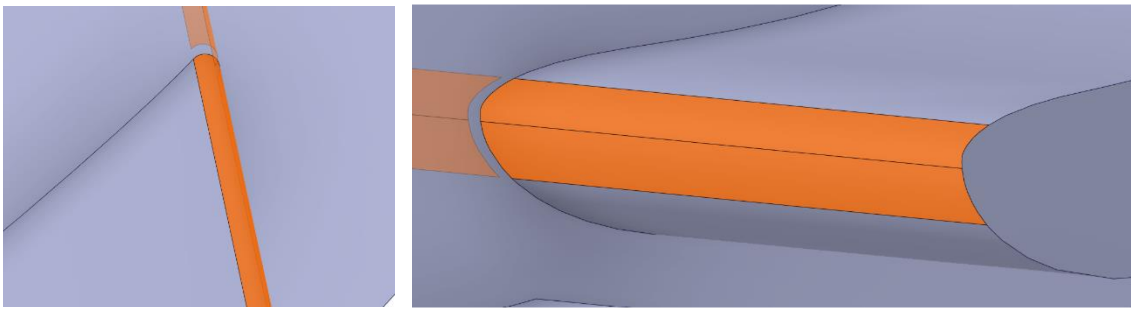

Figure 5-4: Leading & Trailing Edges Close-up

As the study is concentrated on the effect of cornering under event conditions the ground effect needs to be accounted for, therefore, a flat plate has been generated to approximate the front wing in proximity to the ground as best as possible with the resources available for testing, this plate is to the same dimensions as that which would be used within wind-tunnel testing.

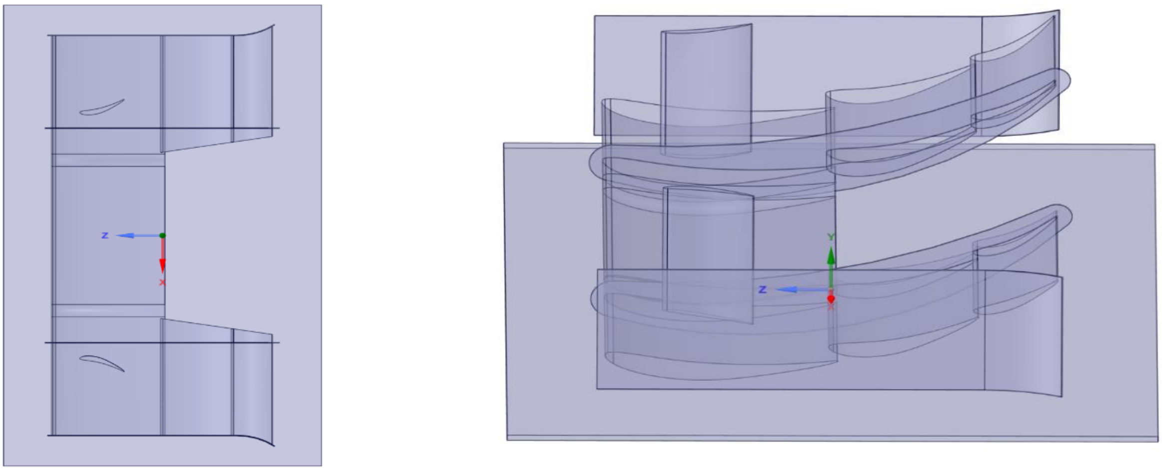

Figure 5-5: Top & Side View of the Geometry in Proximity to the Ground

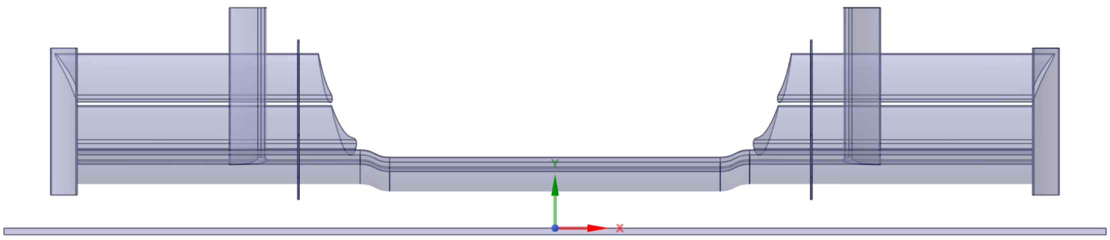

Figure 5-6: Front View of the Geometry in Proximity to the Ground

In order to simulate the effects of yaw the wing was rotated around its centre at variations of 2 degrees for each analysis, this is depicted in figure-5-7 below.

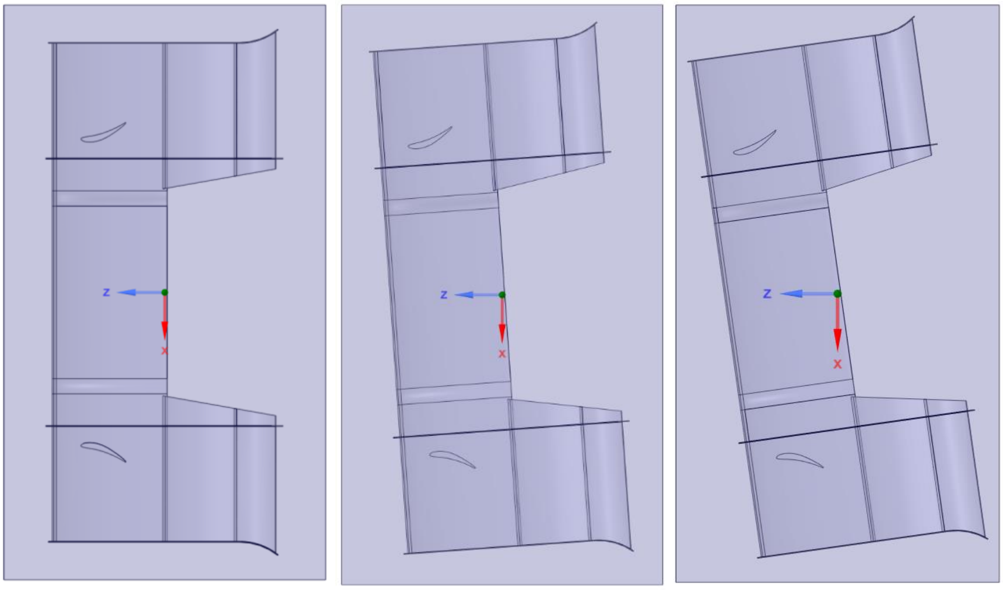

Figure 5-7: Geometry at 0°, 4° & 8° Yaw.

5.1.2. Mesh Analysis

The importance of a mesh analysis is to find the most computationally economical point, where reasonably accurate results can be generated for the lowest number of elements in order to reduce the overall time and computational resources required to run the analysis. Once variations within aerodynamic values reduce to a reasonable level it can be considered that results have become independent of changes within the mesh and further refinement will have little effect on improving accuracy. Minor variations may be made to the geometry when using the same cell count, as they are assumed to have little effect on the accuracy of results.

Tables-5-1 & 5-2 show the values produced for each mesh variation, as well as the percentage change from the previous mesh variant, for both the realizable k-epsilon and k-omega SST models outside of ground effect.

Figures-5-8, 5-9, 5-10 & 5-11 show plots for the force values from each mesh variant, producing a depiction of how the results change as the cell count is increased, thus allowing the reader to visualise how mesh independence is achieved.

A mesh independence study has been performed for the model outside of ground effect at a 0° yaw angle, for increasing cell counts, where initially a course mesh is generated and then further refined for each analysis. For each mesh variation the change in values for lift and drag are compared where it can be seen that after ~$8e^6$ elements the lift and drag values have a variance of less than 1% therefore, it can be assumed that after $8e^6$ elements the results have become independent of changes within the mesh, therefore further analysis can be performed using this cell count.

Initial observations from the mesh independence study shows that the realizable k-epsilon turbulence model with enhanced wall treatment is likely to predict higher lift and drag forces than those predicted by the k-omega SST model.

Table 5-1: K-Epsilon Realizable with Enhanced Wall Treatment Mesh Independence Results				
No. of Elements	5351254	8064926	8720471	15362144
Lift (N)	9.2402	10.198	10.221	10.223
% Change from previous		10.366	-0.226	-0.0196
Drag (N)	1.9923	2.2294	2.2360	2.2372
% Change from previous		11.901	0.296	0.0537

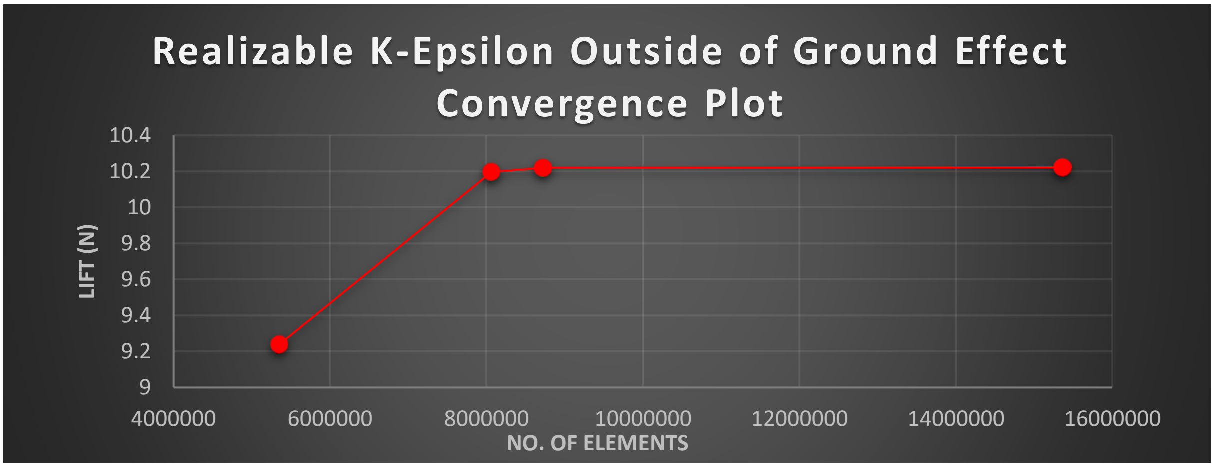

Figure 5-8: Realizable K-Epsilon Model Outside of Ground Effect Convergence Plot for Lift

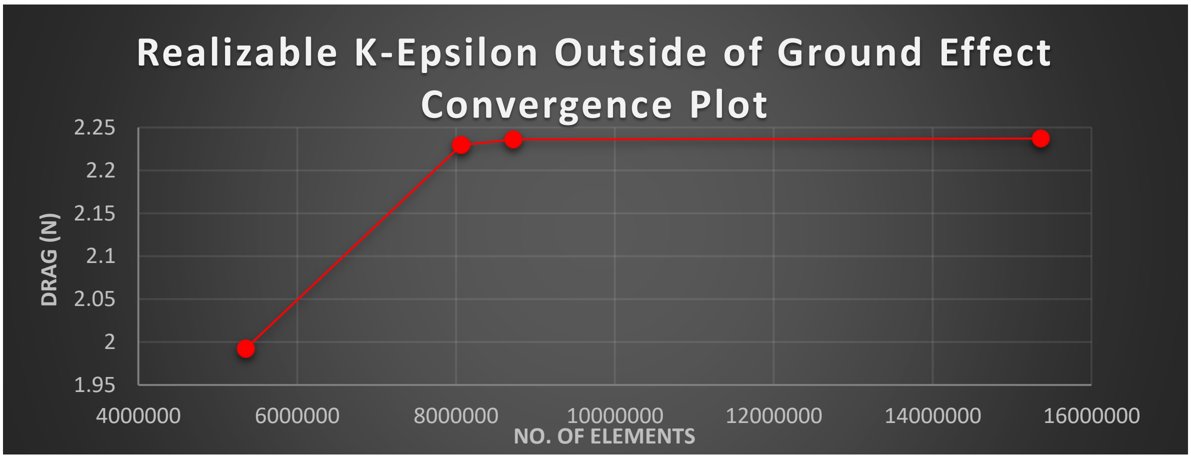

Figure 5-9: Realizable K-Epsilon Model Outside of Ground Effect Convergence Plot for Drag

Table 5-2: K-Omega SST Mesh Independence Results				
No. of Elements	5351254	8055708	8720471	15362144
Lift (N)	9.444	9.339	9.337	9.365
% Change from previous		-1.1112	-0.0214	0.2999
Drag (N)	2.2366	2.3166	2.318	2.3215
% Change from previous		3.5769	0.0604	0.1510

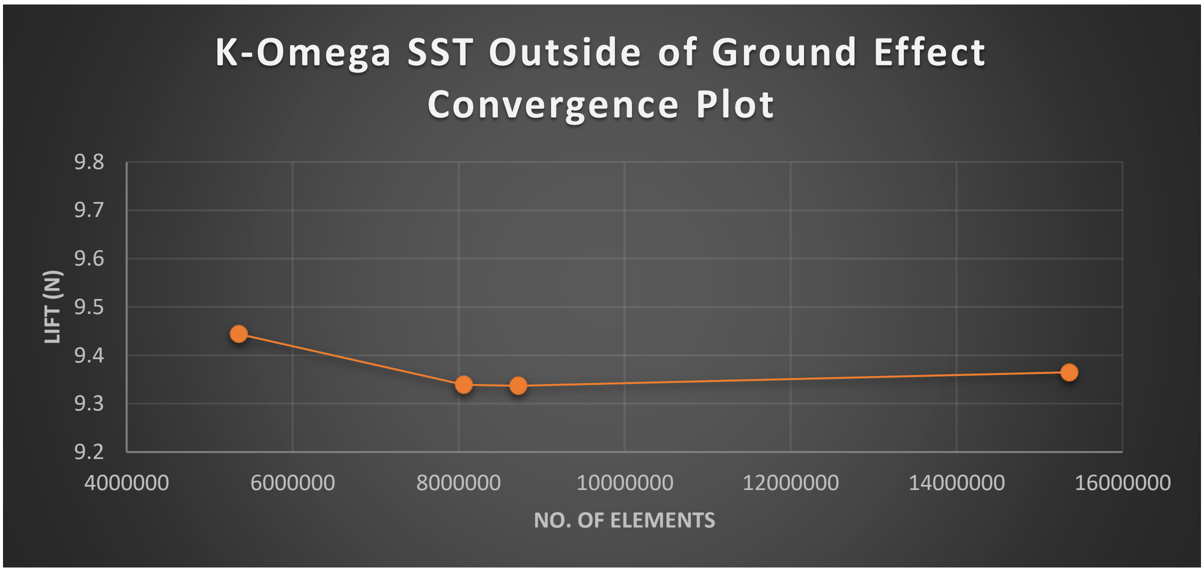

Figure 5-10: K-Omega SST Model Outside of Ground Effect Convergence Plot for Lift

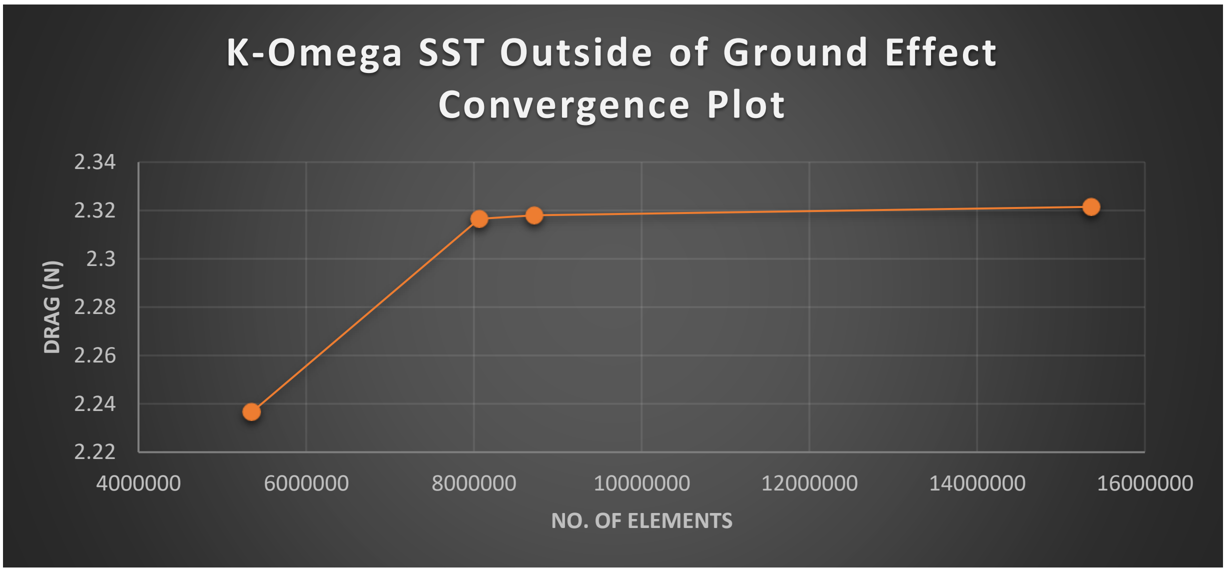

Figure 5-11: K-Omega SST Model Outside of Ground Effect Convergence Plot for Drag

As previously discussed, the calculation for the first layer height and boundary layer thickness required for the generation of inflation layers needed to achieve the desired y+ value is shown in table-5-4 with the variables used within the calculations outlined in table-5-3, the variables used correlate with the default variables used within Ansys Fluent.

Table 5-3: Inflation Layer Variables	
v	30 m/s
ρ	1.225
L	0.1034
μ	$1.7894e^{-5}$
Y+	1

Table 5-4: First Layer Height and Boundary Layer Thickness Values	
Re	212355
C_f	0.004508
τ_w	2.4849
μ_τ	1.4243
y	$1.0256e^{-5}$ m
δ_{99}	0.001102 m

In order to achieve the desired boundary layer thickness, a uniform boundary layer was applied with a growth rate of 1.23 over a total of 15 layers, this resulted in an inflation layer thickness of 0.001112m which encompasses the predicted boundary layer thickness of 0.001102m.

Various sizing functions have been applied to the geometry in order to refine the mesh in areas of higher complexity, such as the leading and trailing edges of the wing, figure-5-12 shows a clipped region of the surface mesh.

Key functions include the body of influence (BOI) surrounding the geometry, which helps refine the enclosure area close to the wing without affecting the bulk of the enclosure, the BOI has been extended up to the outlet as the flow within the wake region is considered to be of high importance, a depiction of this can be seen in figure-5-13.

As discussed previously a prism boundary layer has been applied to the geometry to achieve the desired y+ value, in order to capture the flow effects within the viscous sub-layer, figure-5-14 shows a depiction of the inflation layers applied.

A summary of the mesh settings applied can be found in appendix-12-1.

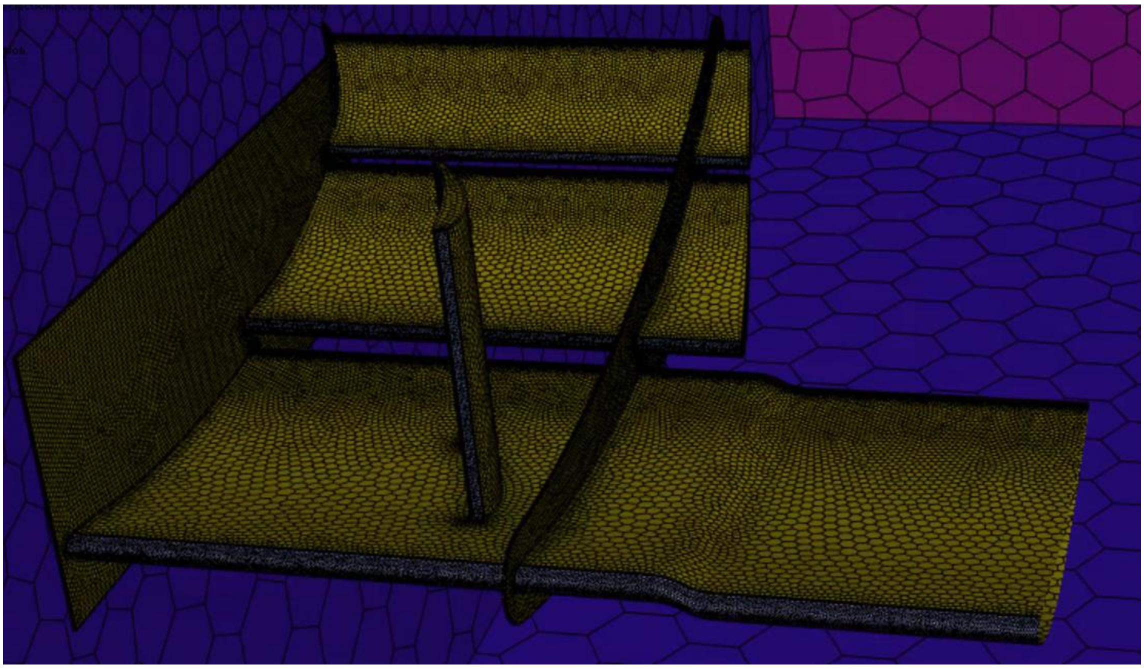

Figure 5-12: Surface Mesh of Clipped Geometry

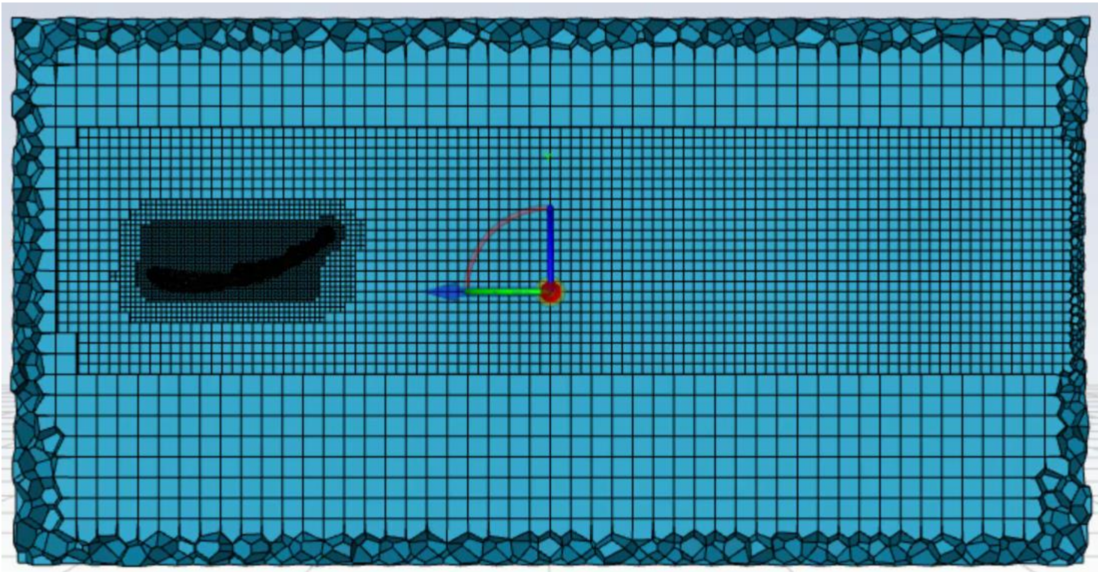

Figure 5-13: Volume Mesh

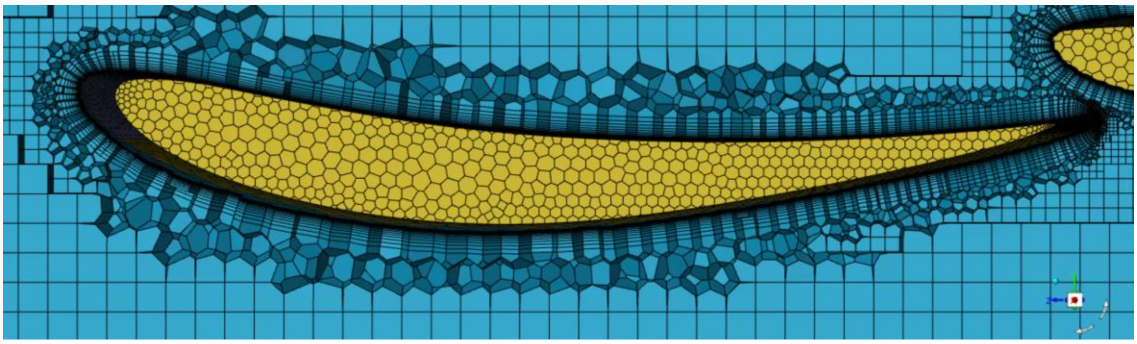

Figure 5-14: Depiction of Inflation Layers Around an Element

Figures-5-15 & 5-16 show a plot of the y+ value vs the position along the wing and a plot of y+ contours across the wing. From these plots it can be observed that the y+ value has been sufficiently reduced to y+~1, where the majority of the wing possesses a y+≤1 with the exception of a few regions along the leading and trailing edges, where refinement could not be reduced without greatly increasing the cell count, the values still remain within suitable limits with the maximum occurring at y+~2.

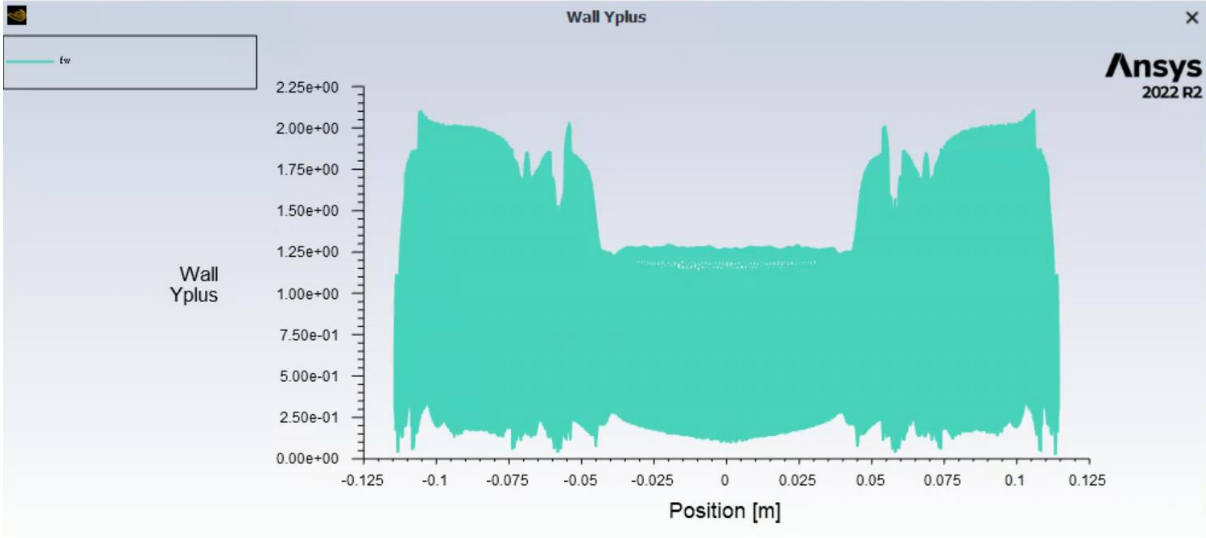

Figure 5-15: Wall y+ Plot Along the Wing

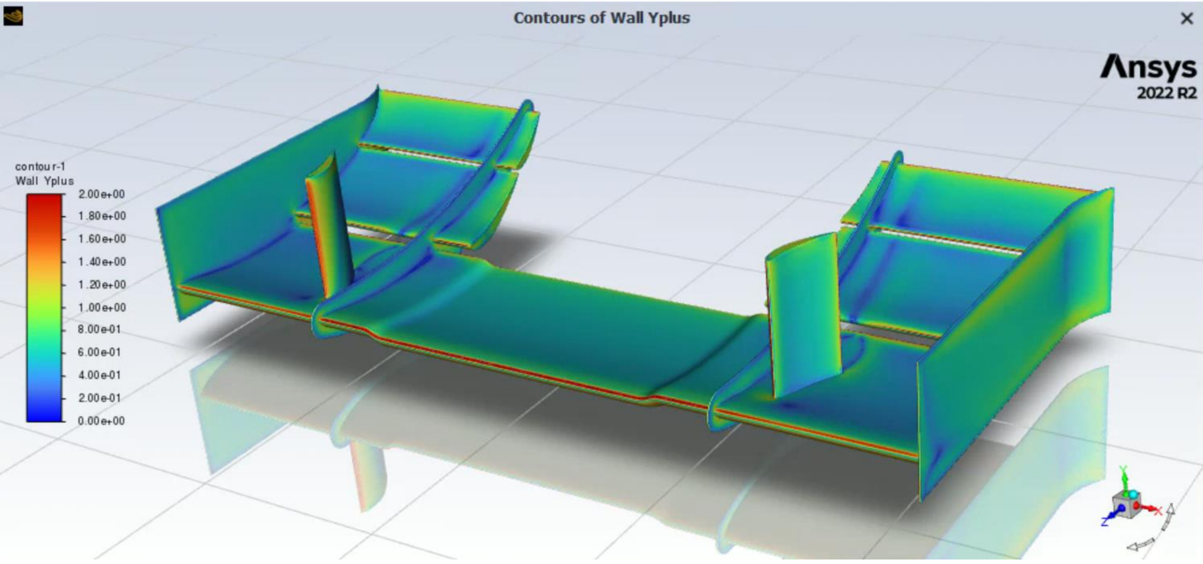

Figure 5-16: Wall y+ Contours Along the Wing

Due to the wind tunnel used in the experimental section, only being able to measure the drag force parallel to the flow direction, for comparative purposes the drag measured in the CFD simulations will also be considered parallel to the flow direction, where in reality the drag would considered parallel to the motion of the wing, thus resulting in the wind tunnel readings showing a combination of drag force and side force.

The quality metrics for orthogonal quality, skewness and aspect ratio, for the mesh produced can be analysed in figures-5-17, 5-18 & 5-19, it can be concluded that the majority of the mesh is of high quality, where the bulk of the mesh lies within the optimal mesh quality regions specified by Ansys, with only a small percentage of the mesh possessing low quality metrics which should have little effect on the accuracy of results.

Mesh setting remain consistent across each analysis leading to little variation in mesh metrics.

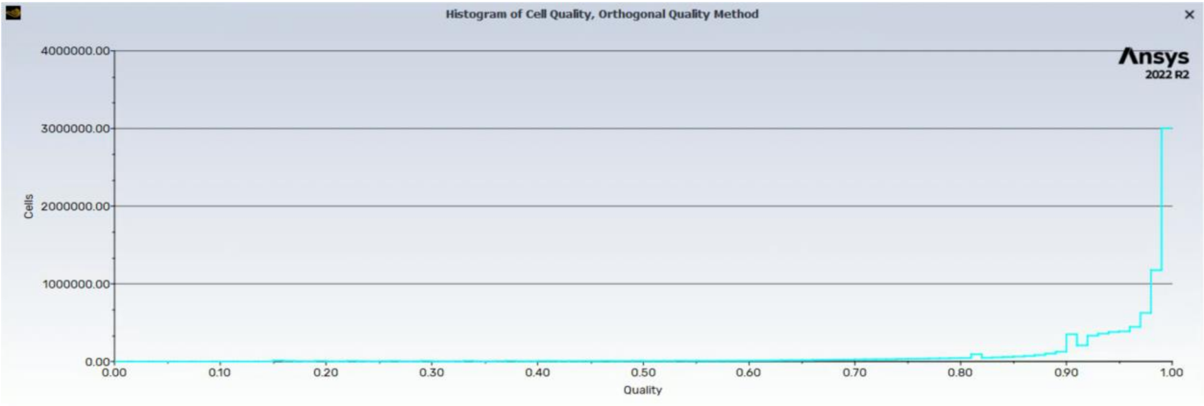

Figure 5-17: Plot for the Mesh Orthogonal Quality

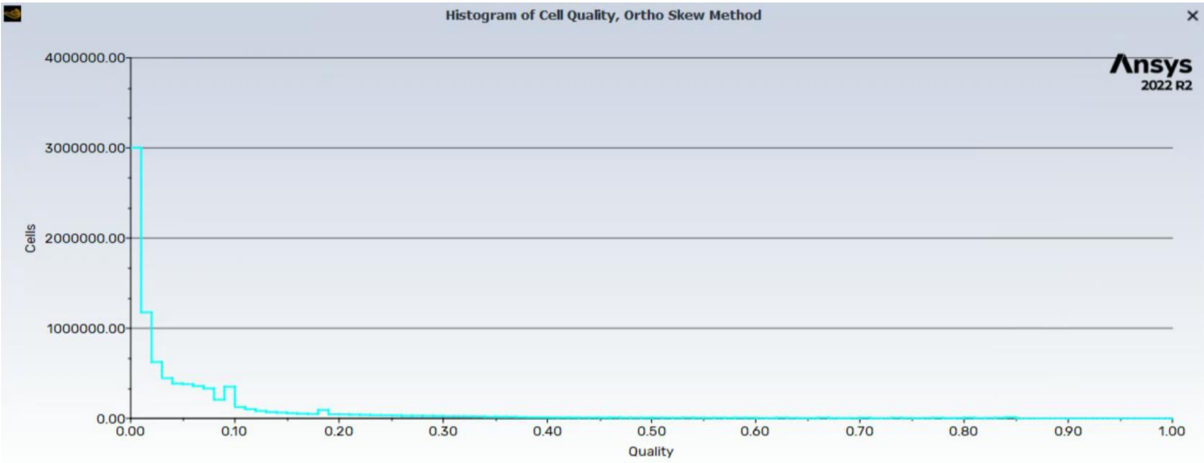

Figure 5-18: Plot for Mesh Skewness

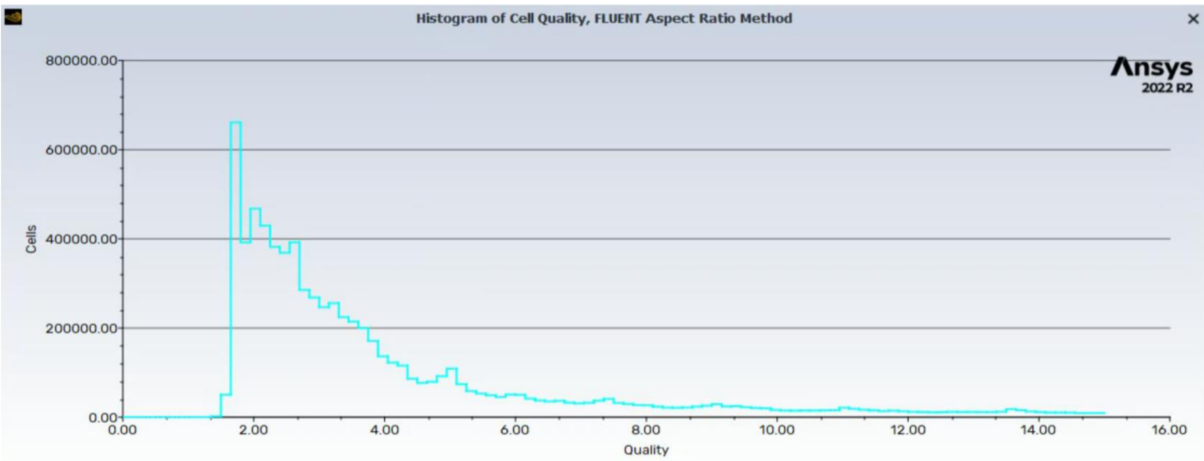

Figure 5-19: Plot for Mesh Aspect Ratio

5.1.3. Boundary Conditions and Setting

Boundary conditions used for both the realizable k-epsilon and k-omega SST models are outline in table-5-5 below, which correlate to the settings required to run the wind tunnel for validation, turbulent intensity and turbulent viscosity ratio have been set based on recommendations from Ansys. These conditions remain constant across all simulations, any unspecified boundary conditions make use of default settings within Ansys Fluent.

Table 5-5: Boundary Conditions	
Velocity inlet	
Velocity Magnitude	30
Turbulent intensity	0.5
Turbulent viscosity ratio	2
Pressure outlet	
Average pressure specification	Applied
Turbulent intensity	0.5
Turbulent viscosity ratio	2

All walls are considered stationary and have a no slip condition applied.

The pressure-velocity coupling makes use of the SIMPLEC scheme with a skewness correction factor of 1 applied to account for any inaccuracies, where recommendations from Ansys state that in complicated flows involving turbulence, the SIMPLEC scheme will improve convergence over the SIMPLE scheme. (ANSYS, 2009)

Spatial discretization was performed to the second order and results were considered converged after residuals reduced by four orders of magnitude.

Table-5-6 shows a summary of the solver methods and monitors used.

Table 5-6: Solver Methods and Monitors	
Pressure-velocity coupling	
Scheme	SIMPLEC
Skewness correction factor	1
Spatial discretization	
Pressure	Second order
Momentum	Second order upwind
Turbulent kinetic energy	Second order upwind
Specific dissipation rate	Second order upwind
Residual convergence criteria	
Continuity	$1e^{-4}$
X, Y, Z velocity	$1e^{-4}$
K	$1e^{-4}$
Epsilon/omega	$1e^{-4}$

5.2. Experimental Procedure

5.2.1. Apparatus

- AF100 sub-sonic open circuit wind tunnel, made up of a silencer, axial fan unit, diffuser, working section and inlet cone (effuser).

- Versatile data acquisition system (VDAS)

- A pitot-static probe positioned upstream, in front of the model. The pitot-static tube has three holes, one at the tip, which is used to measure the stagnation pressure, and two opposite each other in the wall of the pitot tube, these are used to measure the static pressure.

- A standard pitot probe positioned downstream, behind the model is used to measure the downstream pressure.

- Three-component balance

- 1:6 Scaled SHU Racing front wing

(TecQuipment)

5.2.2. Wind Tunnel Model Adaptation

Due to the size and length of the tracks set out during the events at Silverstone, tight cornering conditions mean the vehicles competing are often unable to reach high speeds, in order to approximate the cornering conditions of the event, the analysis is to be performed based on the skid pad event which is composed of a figure eight track layout therefore consisting of an almost constant cornering condition.

Further information on the track layout and IMechE rules can be found in appendix-12.2.

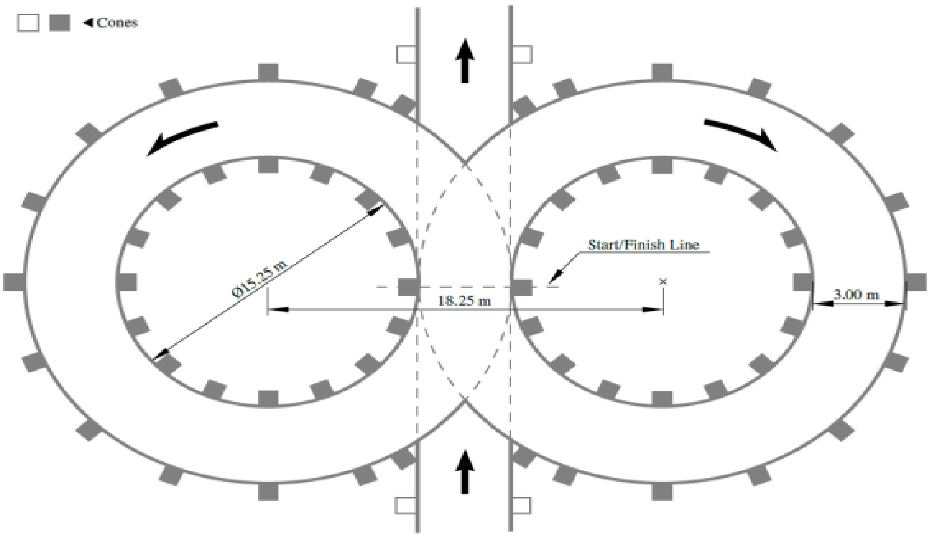

Figure 5-20: IMechE Skid-Pad Layout (IMechE, 2022)

The maximum tangential velocity of the vehicle, without the effects of aerodynamics, while cornering during the skid pad event can be approximated using equation-(33) where the maximum velocity is limited by the frictional contact between the tyres and the ground as well as the radius of the corner, in reality the cornering speed is likely to be higher due to the increased downforce from aerodynamic components, however this provides a good first approximation.

The value calculated for maximum tangential velocity is 8.462m/s, however due to the limitations of the equipment available, it is assumed that the velocity for the vehicle during the event will be 5m/s during the analysis, this is not highly inaccurate as the vehicle is unlikely to travel at the max theoretical velocity.

Equation-(33) is a modified version of the one derived in section-1.4.

$$v_{max} = \sqrt{\mu_s g r} \qquad \dots (33)$$

Due to limitations in terms of the dimensions of the working section of the wind tunnel available, a full-scale model is not able to be tested, therefore scaling of the model is required for the experimental procedure to take place.

Calculations for scaling are performed based on the Reynolds number, where the Reynolds number and kinematic viscosity are assumed to remain constant during actual and experimental conditions, the scale of the model is decided based on the ratio of the velocity of the vehicle in actual conditions vs the wind speed used for the experimental procedure.

$$\frac{u_{actual}L_{actual}}{v_{actual}} = \frac{u_{exp}L_{exp}}{v_{exp}} \rightarrow \frac{u_{actual}}{u_{exp}} = \frac{L_{actual}}{L_{exp}} \qquad \dots (34)$$

With the maximum wind speed of the wind tunnel being limited to 36m/s, a decision was made to run the experiment at ~30m/s allowing the model to be scaled by 1:6, as well as providing operating room in terms of variations in ambient conditions, which could affect the operating Reynolds number. A scale of 1:6 also maximises the model size reducing the difficulties of 3D printing due to small scale features, while staying within the limits of the working section, the blockage ratio was ~5.2% which is within reasonable limits for this type of testing.

The model was scaled in SolidWorks and printed using the SHU Tri-Tech resin printer, where resin is used as a support for floating geometry, allowing for small scale features to be printed accurately without the need for polymer supports which would otherwise affect the surface quality.

A stand was designed and printed on the model, which allows the user to attach the model to a flat plate, which acts as the ground in this scenario and relays the forces impacting the wing through the three-component balance, while also providing indicators of the yaw position, where a pin can be used to align the desired position.

Figure 5-21: Experimental 3D Printing Model Adaptation

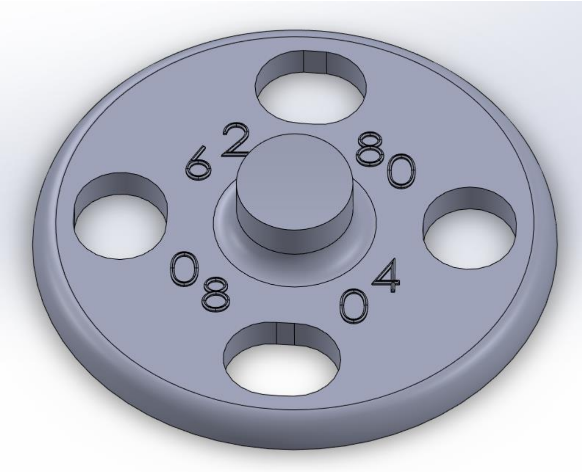

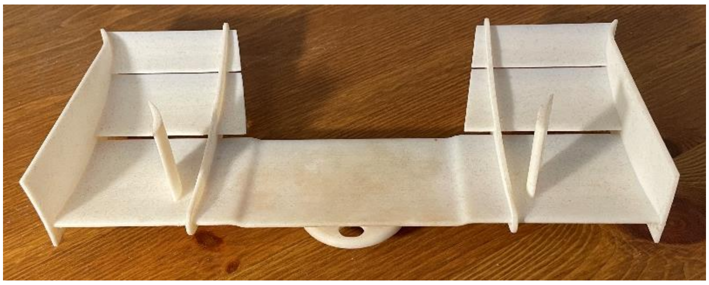

Figure 5-22: Model Used in the Experimental Study

Figure 5-23: Experimental Stand

5.2.3. Procedure

The experimental procedure was performed in a low-speed open loop, sub sonic wind tunnel, where drag and lift forces are measured using a three-component balance, which relays the forces generated through a cable system and where they are then measured by strain gauge load cells and recorded by the VDAS system.

Wind speed is calculated by the VDAS system using the pitot static tube, where dynamic pressure is calculated from the total and static pressure, while wind speed is calculated from the dynamic pressure.

After calibration procedures were performed and the experimental setup was complete, ambient conditions were recorded and entered into the VDAS system.

The wind speed was adjusted until a chord-based Reynolds number of $\sim 2e^5$ was achieved in correlation with the CFD analysis performed, after which wind speed was fixed.

In order to capture results the model was adjusted to the desired yaw angle before running the wind tunnel, additionally before recording results the wind tunnel was allowed to run until fluctuations in readings settled to a reasonable level, after which the VDAS system was used to record results over a span of 2 minutes, where 120 readings for lift and drag force values were recorded, an average of the 120 recordings was taken as the mean value for lift and drag to account for any disturbances or fluctuations during the procedure.

Figure 5-24: AF100 SHU Wind Tunnel

6. Results

6.1. CFD Results

For the purpose of this report, the positive directions considered for the force vectors are displayed below in figure-6-1.

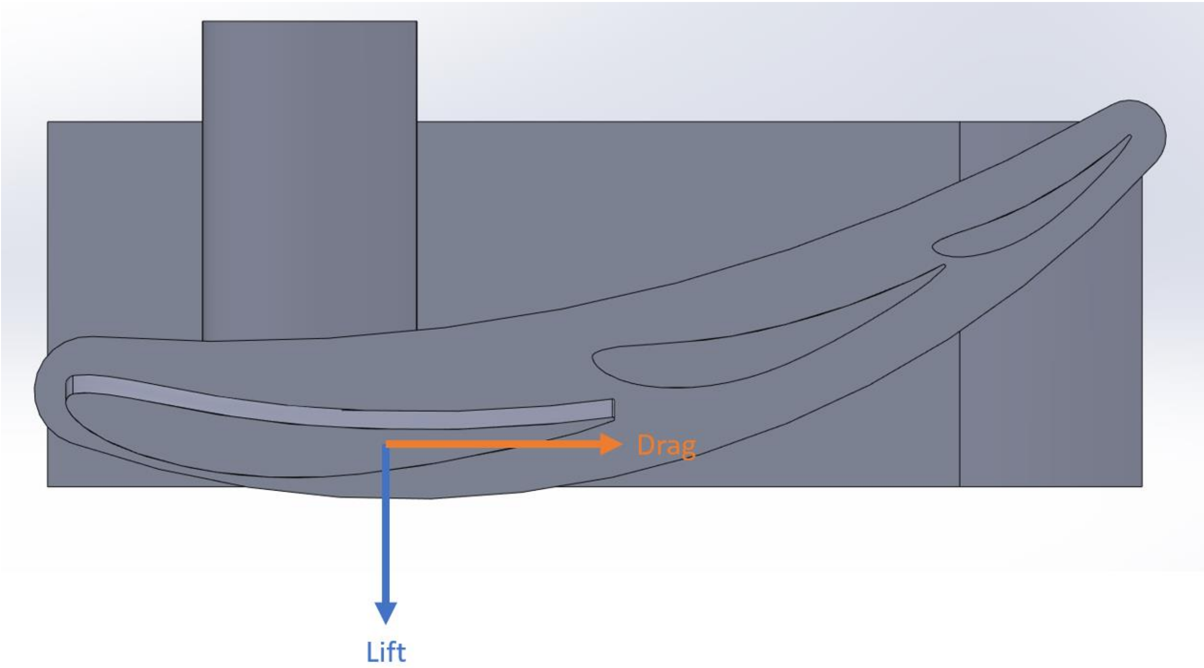

Figure 6-1: Positive Force Directions

Approximations for the lift and drag forces, from the CFD simulations, for the realizable k-epsilon and k-omega SST turbulence models are shown in tables-6-1 & 6-2, and the realizable k-epsilon outside of ground effect shown in table-6-3, where the 0° yaw angle may be considered the baseline for each set of results. In addition to these properties the percentage change in force value between each yaw variant, and percentage change in force value from the baseline have been displayed.

Plots for the lift and drag forces against yaw angle, from each simulation, are displayed below each table and it can be seen for each plot a gradually decreasing slope for lift is produced as the yaw angle is increased, while the opposite effect occurs for drag where an almost exponential increase in drag occurs as yaw angle increases.

The k-omega SST model has been used to perform approximations at 0°, 4° & 8° yaw for comparison against the realizable k-epsilon model. Results show a difference in predictions for lift, with the k-omega model predicting lower force values, however the overall change in lift is similar with the k-omega model showing a much more gradual decrease in lift for changing yaw angle.

The values predicted for drag are not too dissimilar however, the k-omega model predicts a much greater percentage change for each yaw variation compared to the k-epsilon model.

6.1.1. Realizable K-Epsilon

Table 6-1: Realizable K-Epsilon Results

Yaw angle (deg)	0	2	4	6	8
Lift (N)	12.819	12.814	12.793	12.758	12.717
% change from previous		-0.0390	-0.1639	-0.2736	-0.3214
% change from 0°		-0.0390	-0.2028	-0.4759	-0.7957
Drag (N)	2.6806	2.6817	2.6957	2.7169	2.7557
% change from previous		0.0410	0.5221	0.7864	1.4281
% change from 0°		0.0410	0.5633	1.3542	2.8016

Figure 6-2: Realizable K-Epsilon Lift Vs Yaw Angle Plot

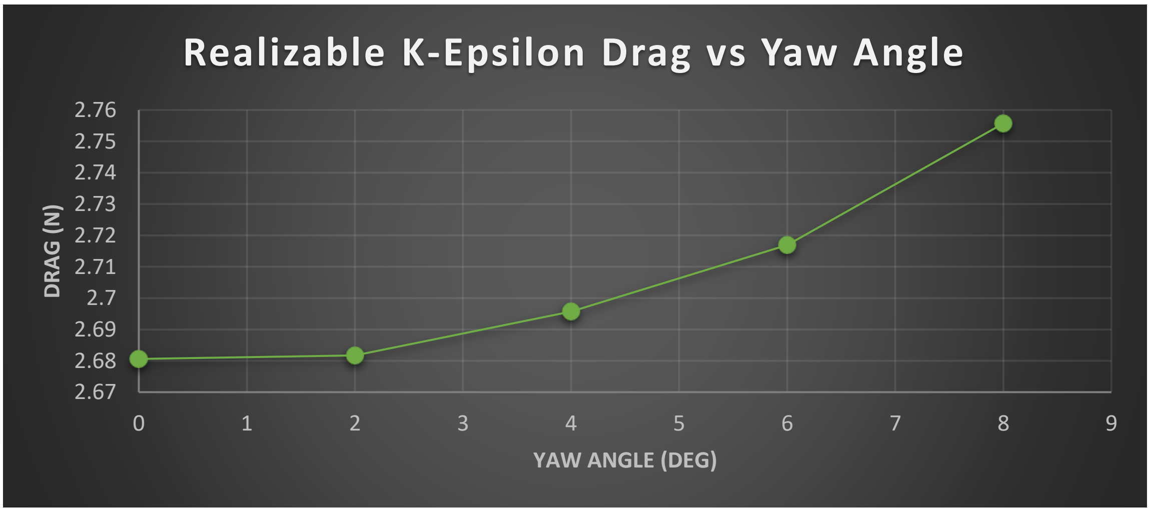

Figure 6-3: Realizable K-Epsilon Drag vs Yaw Angle Plot

6.1.2. K-Omega SST

Table 6-2: K-Omega SST Results

Yaw angle (deg)	0	4	8
Lift (N)	10.768	10.765	10.687
% change from 0°		-0.0279	-0.7522
Drag (N)	2.4684	2.4913	2.5832
% change from 0°		0.9277	4.6508

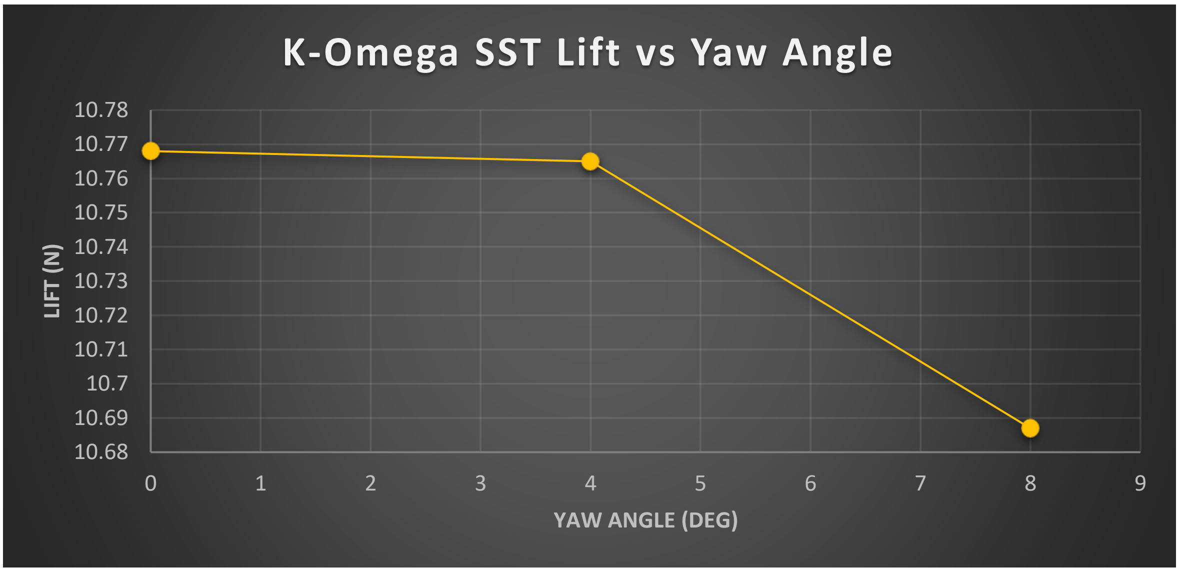

Figure 6-4: K-Omega SST Lift vs Yaw Angle Plot

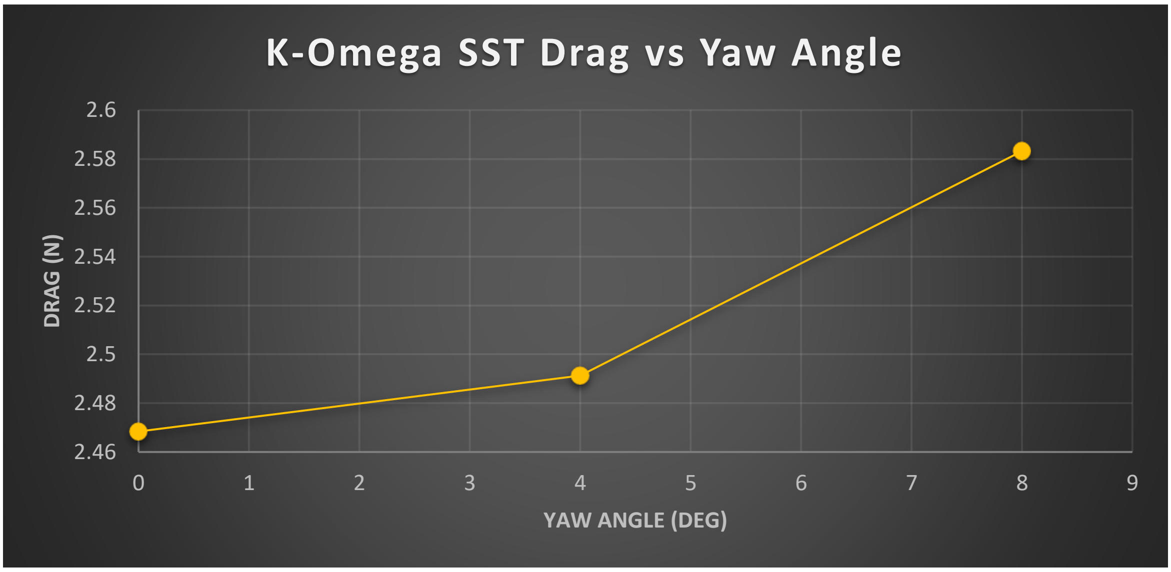

Figure 6-5: K-Omega SST Drag vs Yaw Angle Plot

6.1.3. Realizable K-Epsilon Outside of Ground Effect

Table 6-3: Realizable K-Epsilon Outside of Ground Effect Results					
Yaw angle (deg)	0	2	4	6	8
Lift (N)	9.999	9.997	9.993	9.984	9.967
% change from previous		-0.0200	-0.0400	-0.0901	-0.1703
% change from 0°		-0.0200	-0.0600	-0.1500	-0.3200
Drag (N)	2.557	2.5612	2.5785	2.6074	2.6527
% change from previous		0.1643	0.6755	1.1208	1.7374
% change from 0°		0.1643	0.8408	1.9711	3.7427

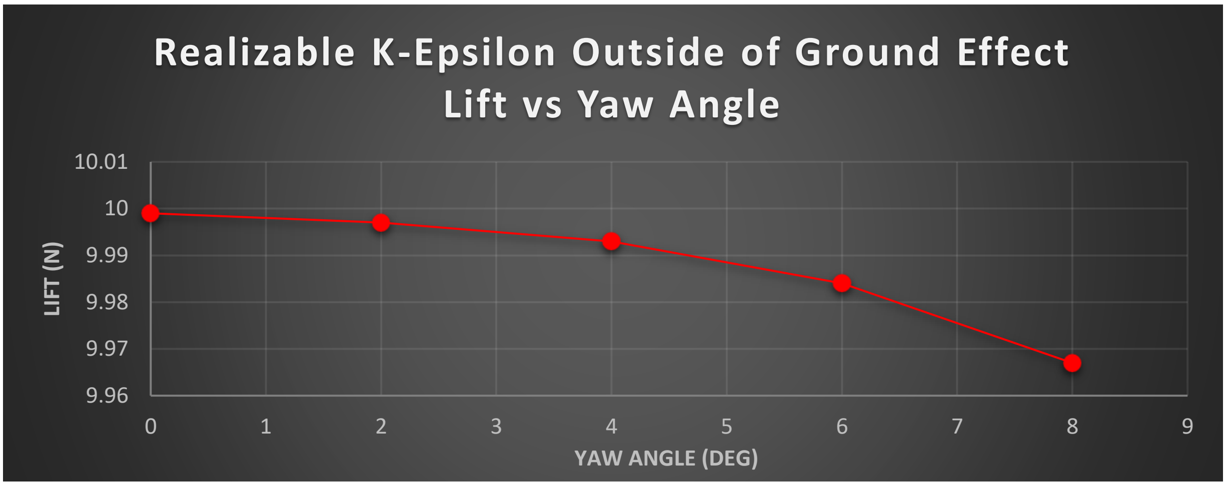

Figure 6-6: Realizable K-Epsilon Outside of Ground Effect Lift vs Yaw Angle Plot

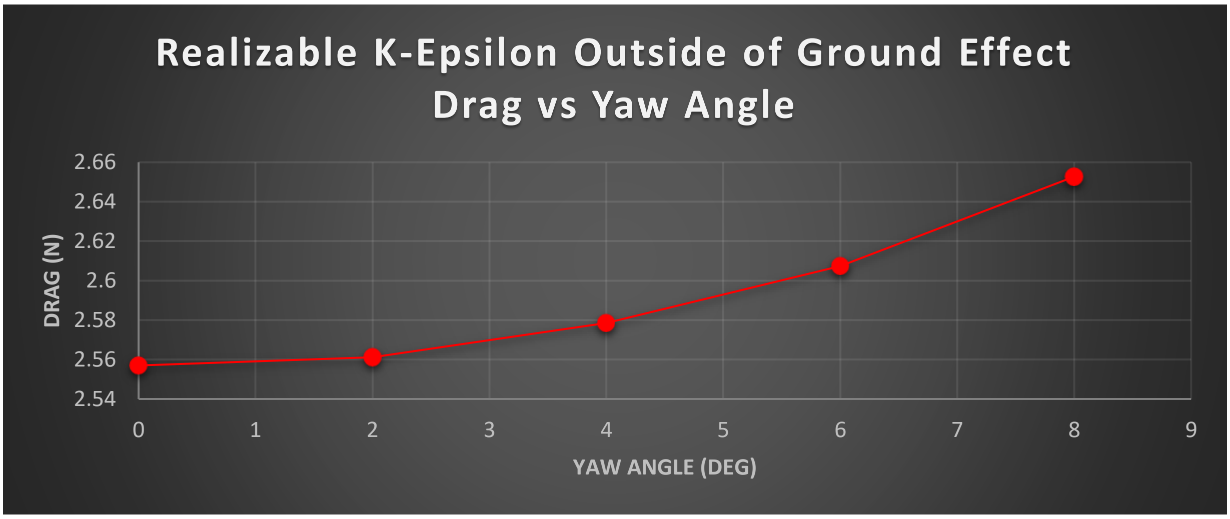

Figure 6-7: Realizable K-Epsilon Outside of Ground Effect Drag vs Yaw Angle Plot

6.2. Experimental Results

Averaged data from the experimental procedure is shown in table-6-4 with plots for the lift and drag forces below, strong correlation to the CFD data in terms of plot trends can be seen with a full comparison being made shortly.

Table 6-4: Wind Tunnel Results

Yaw angle (deg)	0	2	4	6	8
Lift (N)	10.922	10.906	10.854	10.798	10.699
% change from previous		-0.1442	-0.4806	-0.5129	-0.9153
% change from 0°		-0.1442	-0.6241	-1.1338	-2.0387
Drag (N)	3.4283	3.4300	3.4388	3.4752	3.5198
% change from previous		0.0486	0.2551	1.0005	1.3436
% change from 0°		0.0486	0.3038	1.3073	2.6685

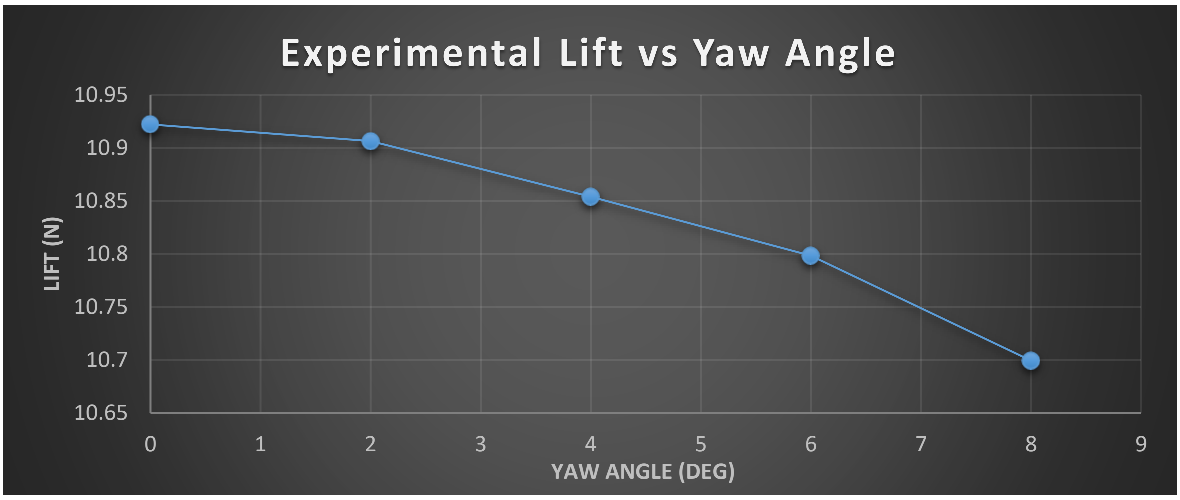

Figure 6-8: Experimental Lift vs Yaw Angle Plot

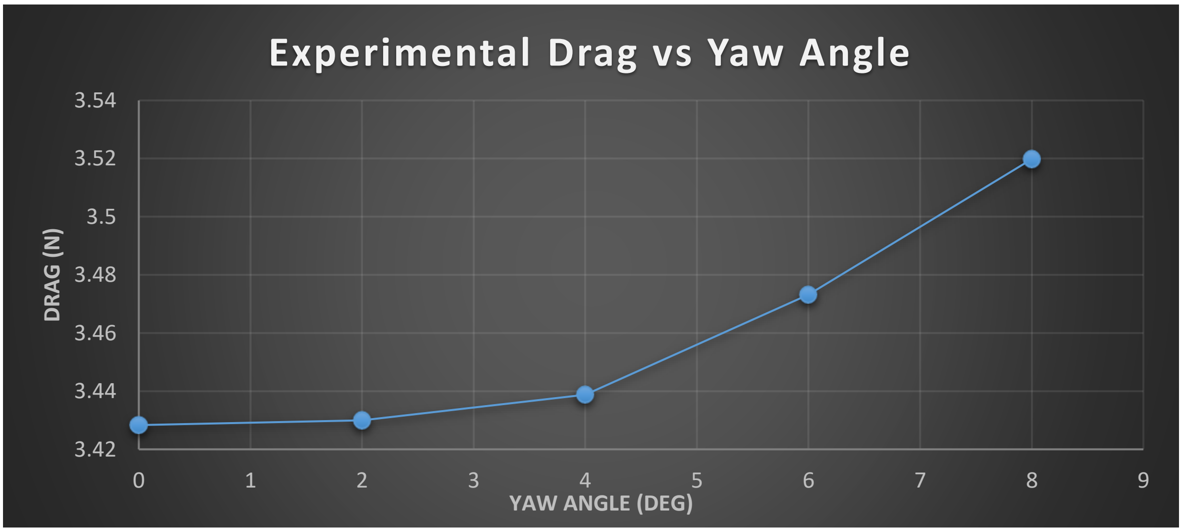

Figure 6-9: Experimental Drag vs Yaw Angle Plot

6.3. Comparison

In comparison to the experimental data, strong correlation in terms of trends can be seen however, predictions for lift are much higher for the k-epsilon model when compared to the experimental data, while the k-omega model shows close relations in terms of values compared to the experimental data.

Predictions for drag from both models are much lower compared to those in the experimental data, likely pointing towards interaction between the stand and the flow across the model in the experimental setup, which could be causing increased drag with a slight reduction in lift.

The simulations performed outside of ground effect show clear reductions in lift and drag however, the k-omega model in ground effect predicts a lower drag when compared to the realisable k-epsilon model outside of ground effect, this combined with the previous observations point towards the k-omega model under-predicting lift and drag forces while, the k-epsilon model may over predict lift and drag forces, this correlates with the observation made in the mesh analysis section.

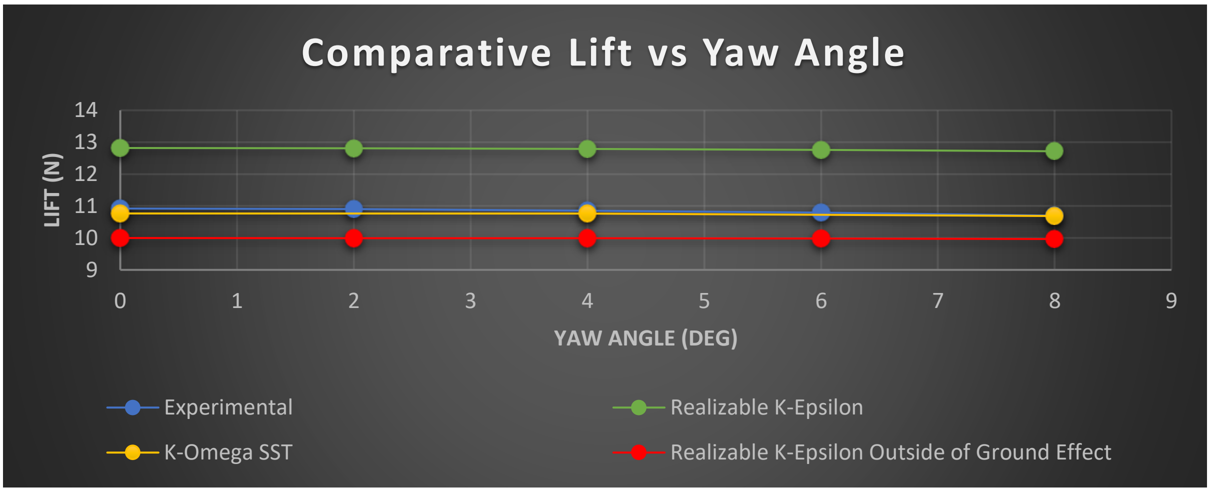

Figure 6-10: Comparative Lift vs Yaw Angle Plot

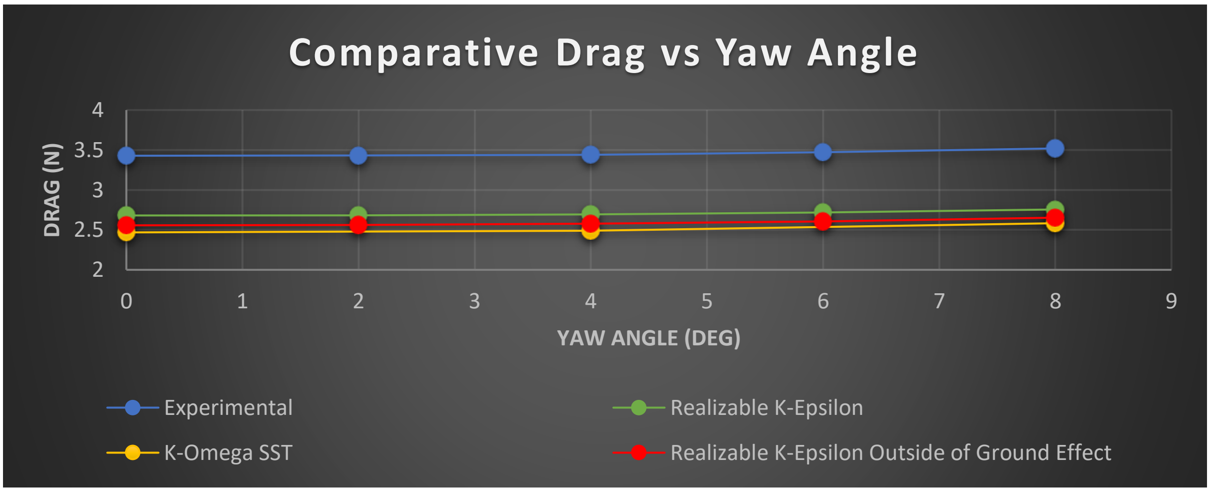

Figure 6-11: Comparative Drag vs Yaw Angle Plot

6.4. Drag and Side Force Relative to the Wing

This section observes the drag and side force vectors acting relative to the wing, where previously the drag force was approximated as a combination of drag and side forces acting parallel to the airflow for comparison against the experimental data.

The drag and side forces acting in relation to the wing, from the realizable k-epsilon model, are displayed in table-6-5 as well as plotted in figures-6-12 & 6-13.

Observations show that an almost linear decrease in drag is apparent when increasing yaw, with slight deviations at 4° & 6° likely due to mesh variance or flow interactions, the deviation is however minor. This observation is dissimilar to the drag parallel to the flow direction, which showed almost exponentially increasing drag with increasing yaw angle.

The side force shows the opposite effect where an almost linear increase in force can be seen for increasing yaw angle.

Table 6-5: Drag and Side Force Results Relative to the Wing

Yaw angle (deg)	0	2	4	6	8
Drag Component (N)	2.6806	2.6763	2.6734	2.6653	2.6633
% change from previous		0.1231	0.7787	1.2555	2.0352
% change from 0°		0.1231	0.9028	2.1697	4.2490
Side Force Component (N)	-0.0168	0.2016	0.4120	0.6334	0.8503
% change from previous			104.3734	53.7337	34.2360

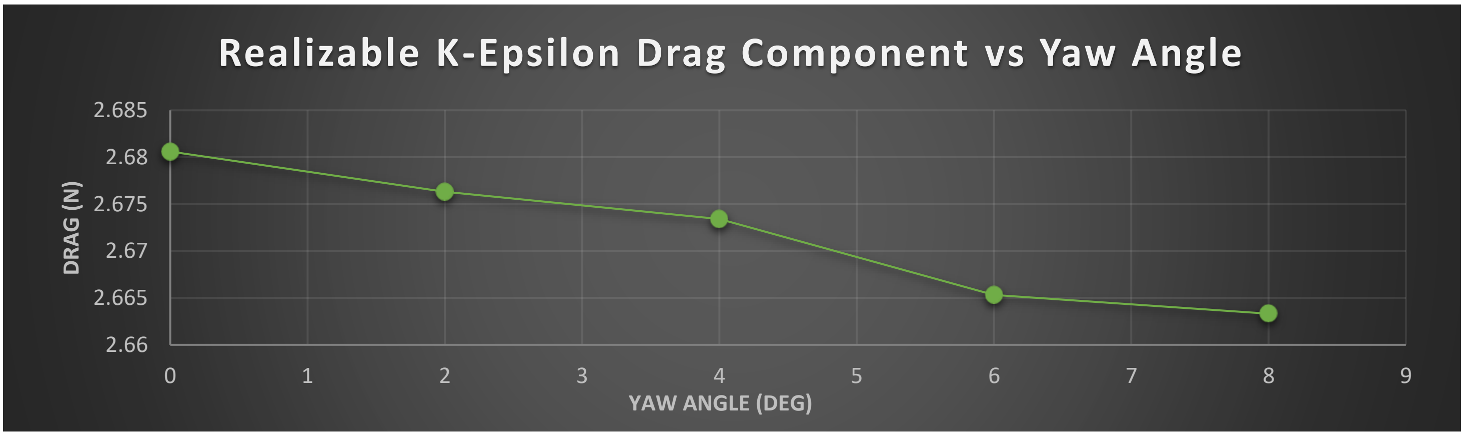

Figure 6-12: Realizable K-Epsilon Drag Component vs Yaw Angle Plot

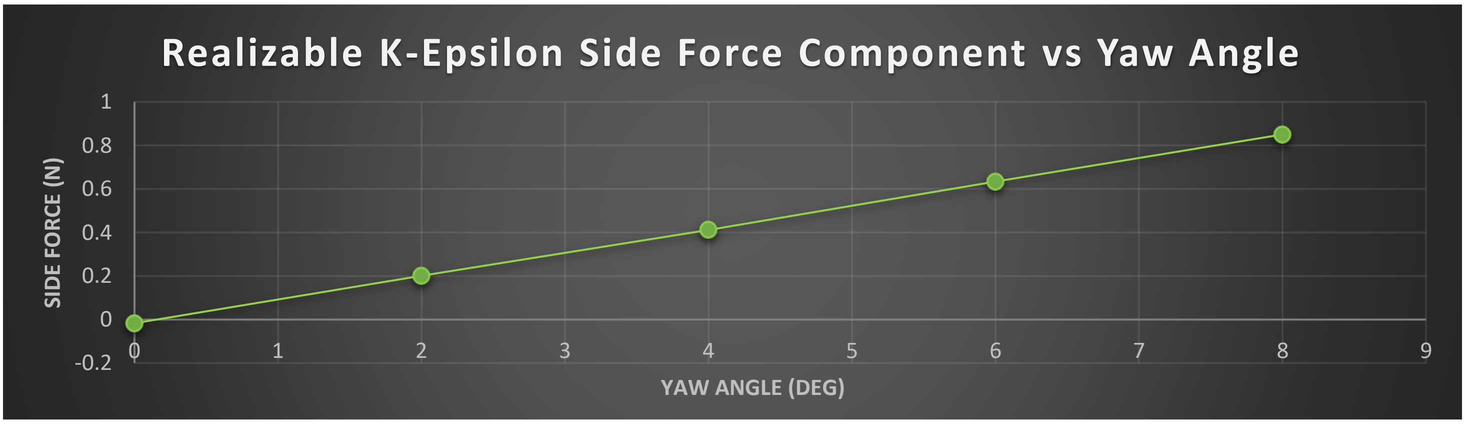

Figure 6-13: Realizable K-Epsilon Side Force Component vs Yaw Angle Plot

6.5. Contour Plots

Contour plots for static pressure, velocity magnitude and turbulent intensity, for the realizable k-epsilon model, at 0°, 4° and 8° yaw angles are shown below, where all plots use the same scale for easy comparability, as well as the baseline having symmetrical flow properties on either side of the wing.

Figure-6-14 & 6-15 show the plane positions used to produce the contour plots, with static pressure and velocity magnitude being shown on the planes in figure-6-14 positioned around the mid-section of the left and right element cascades, while the turbulent intensity contours are produced on the planes in figure-6-15 positioned around the leading, trailing and midsection of the wing, to show how turbulent intensity is built up as flow progresses along the wing.

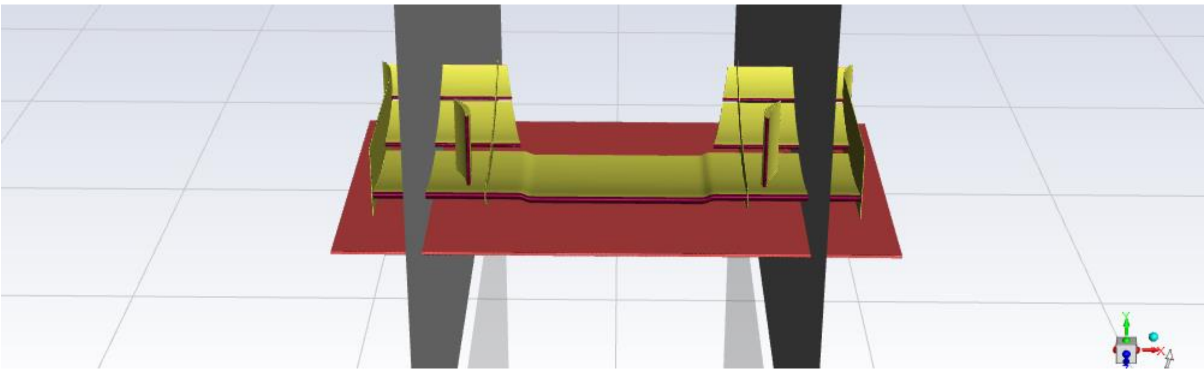

Figure 6-14: Contour Planes Positioned on the Cascades

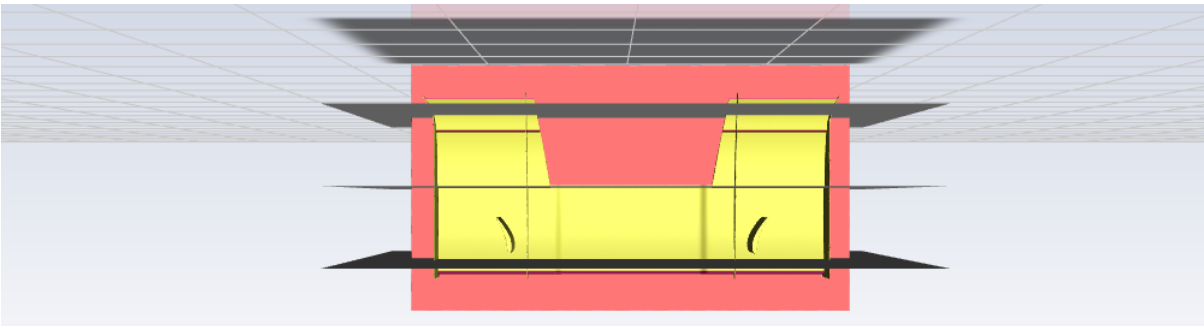

Figure 6-15: Contour Planes Positioned Along the Wing

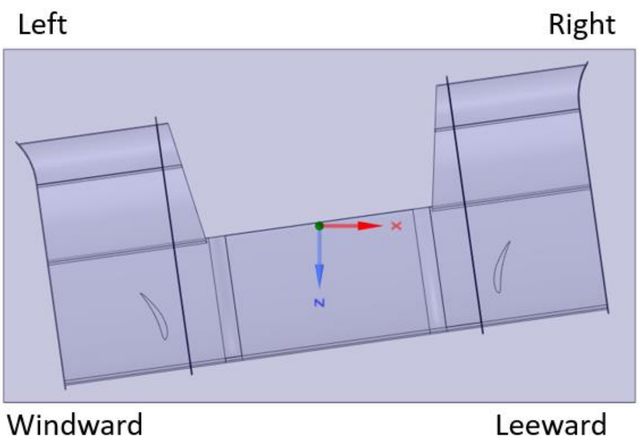

Figure 6-16: Depiction of the Windward and Leeward Sides

6.5.1. Static Pressure Plots

Contour plots for static pressure shown below, display how static pressure changes with varying yaw angle, the baseline plot shows, as expected, a high-pressure region close to the upper surface of the aerofoil, with a low-pressure region below the aerofoils, observing the low-pressure region extending from the aerofoil in closer proximity to the ground due to the ground proximity.

Compared to the baseline, the windward side shows an increase in pressure below the wing, with minimal effects in the wake region, while the leeward side shows a decrease in pressure below the wing, with a minor increase in pressure in the wake region, very little change in the pressure is seen above the wing on either side.

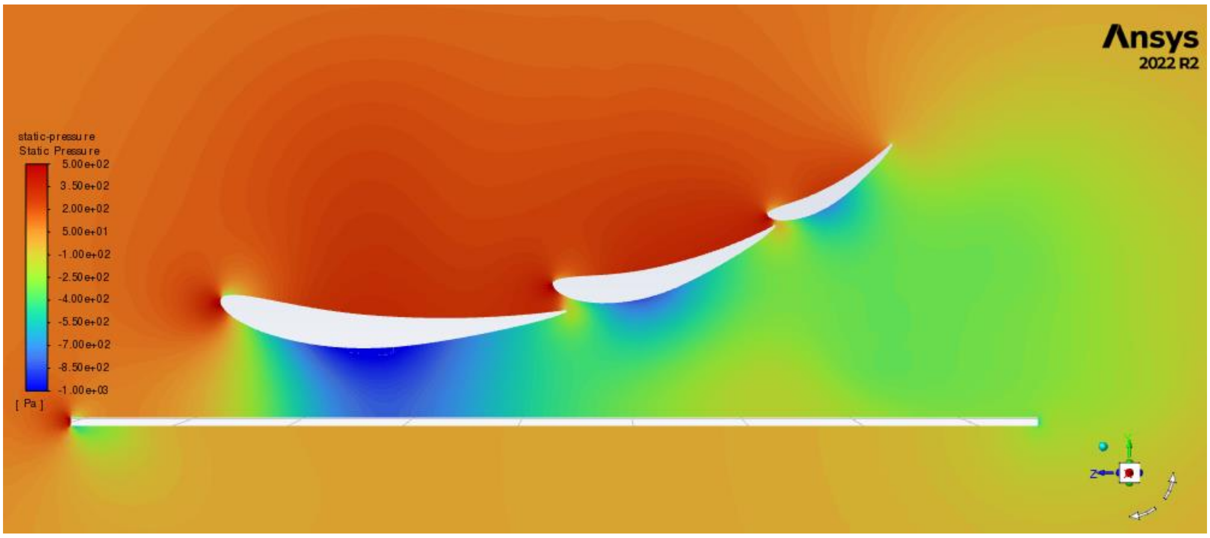

Figure 6-17: Baseline Static Pressure Contour

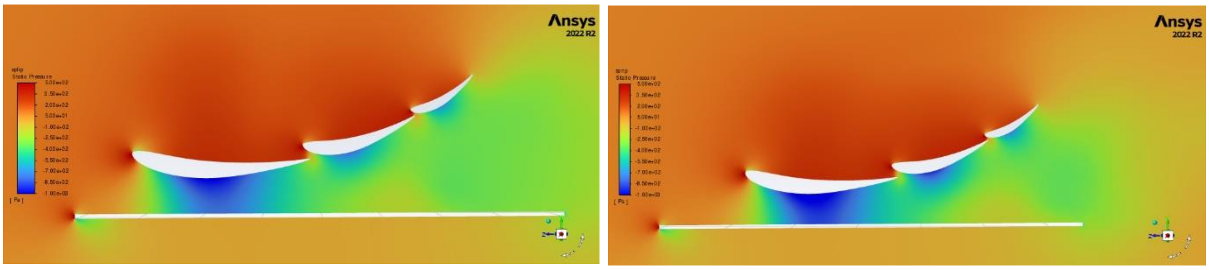

Figure 6-18: 4° Static Pressure Contours, Windward & Leeward

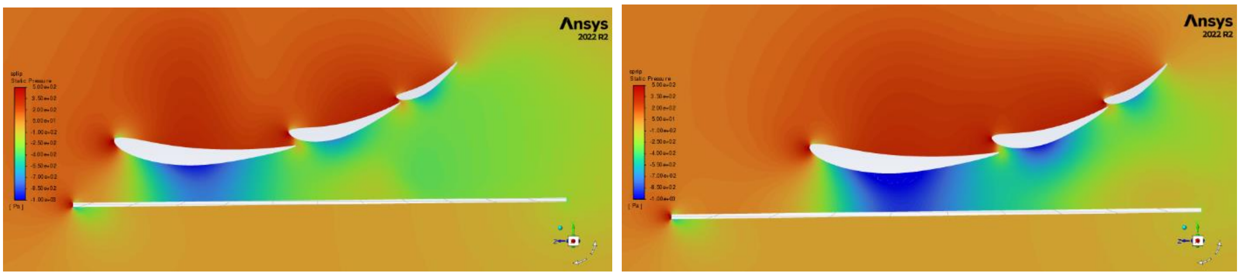

Figure 6-19: 8° Static Pressure Contours, Windward & Leeward

6.5.2. Velocity Magnitude Plots

Contour plots for velocity magnitude shown below, display how the magnitude of velocity changes with varying yaw angle, the baseline plot shows the large difference in flow velocity between the upper and lower surface of the aerofoil, where the flow below the aerofoil is almost doubled. Additionally, an area of low velocity can be seen extending in the wake region.

Compared to the baseline, the windward side experiences a minor reduction in flow velocity below the elements, however the main variation is the growth of the low velocity area in the wake region.

The leeward side compared to the baseline, shows a minor increase in flow velocity below the elements, while the low velocity region experiences the opposite effect to the windward side, where the region gradually decreases with yaw angle.

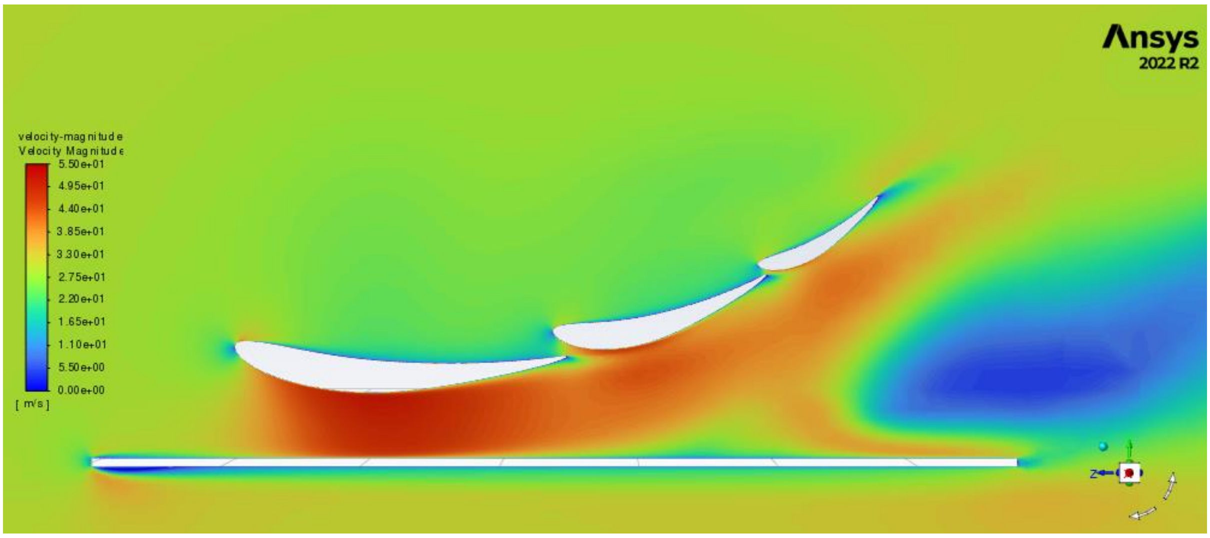

Figure 6-20: Baseline Velocity Magnitude Contour

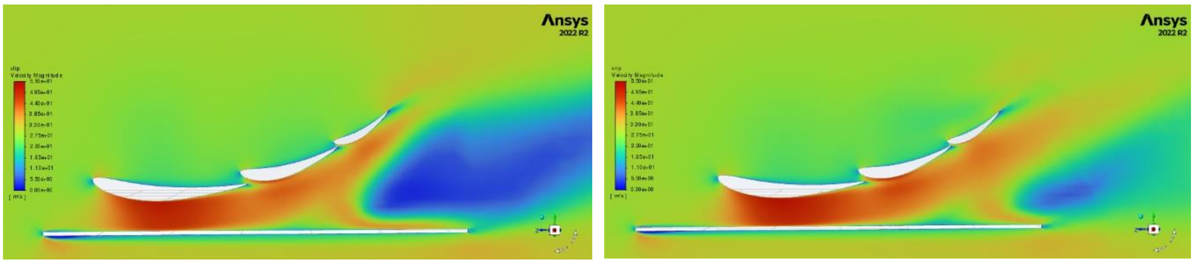

Figure 6-21: 4° Velocity Magnitude Contours, Windward & Leeward

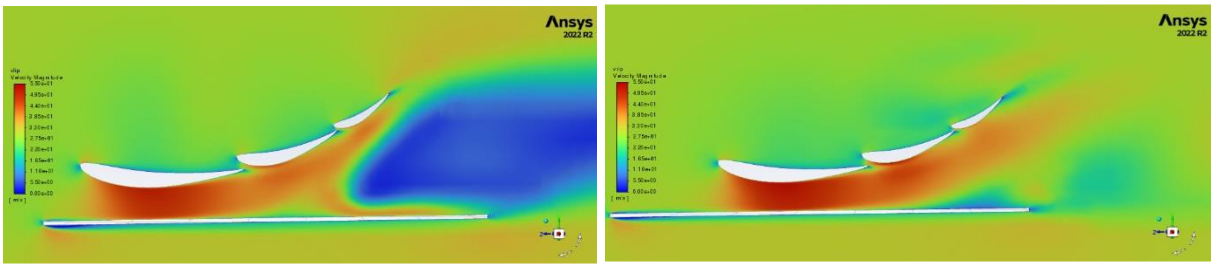

Figure 6-22: 8° Velocity Magnitude Contours, Windward & Leeward

6.5.3. Turbulent Intensity Plots

Contour plots for turbulent intensity shown below, display how the turbulent intensity progresses along the wing, on the windward and leeward side, with varying yaw angles. The baseline plot shows an increase in turbulent intensity towards the rear of the wing, this is likely the cause of the low velocity region analysed in the velocity magnitude plots, where eddies are likely being generated towards the rear of the wing.

Compared to the baseline, the windward side experiences an increase in turbulent intensity within the turbulent region, where the turbulent bubble increases in size and magnitude.

The leeward side compared to the baseline, shows a gradual decrease in turbulent intensity within the turbulent region, where the turbulent bubble gradually decreases in both size and magnitude. Turbulent activity does however increase within the mid-section of the wing.

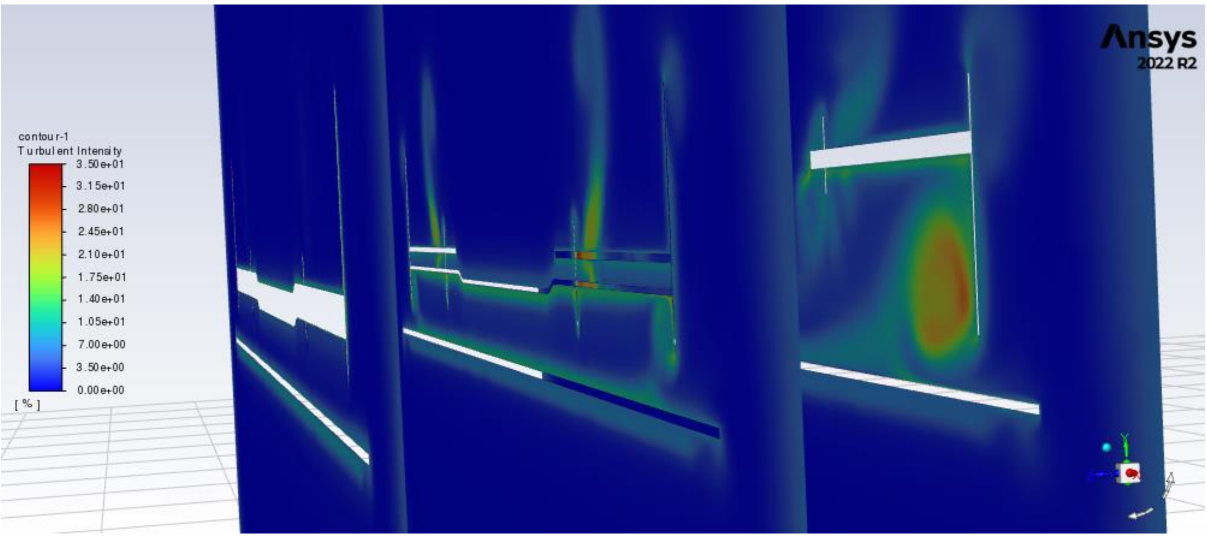

Figure 6-23: Baseline Turbulent Intensity Contour

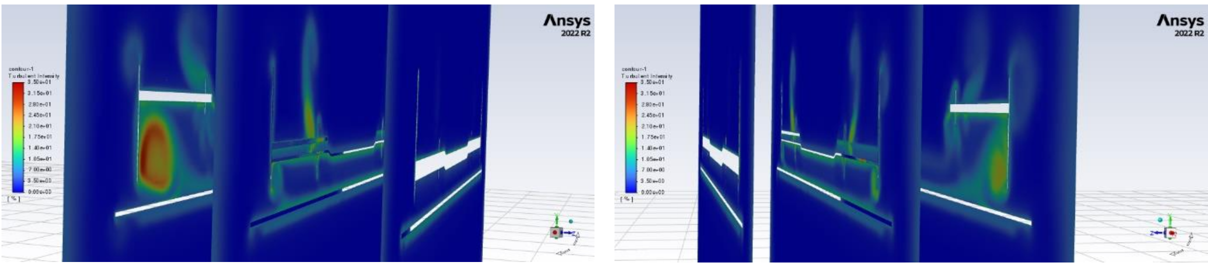

Figure 6-24: 4° Turbulent Intensity Contours, Windward & Leeward

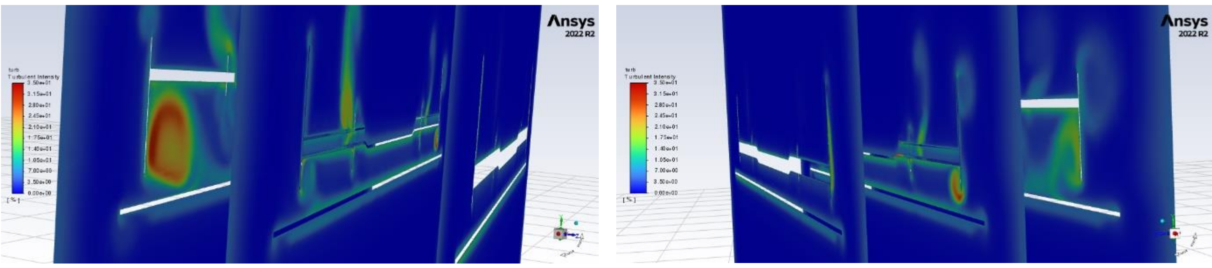

Figure 6-25: 8° Turbulent Intensity Contours, Windward & Leeward

6.5.4. Outside of Ground Effect

Contour plots for static pressure, velocity magnitude and turbulent intensity for the baseline of the realisable k-epsilon model outside of ground effect, are shown below. Comparing the plots to the baseline of the same model in ground effect, it can clearly be seen that a lack of ground effect causes an increase in static pressure, as well as decreased velocity below the elements, the low velocity wake region is also no longer visible. The turbulent intensity contours show diminished turbulent activity compared to the model in ground effect, where the turbulent region towards the rear of the wing has almost entirely faded.

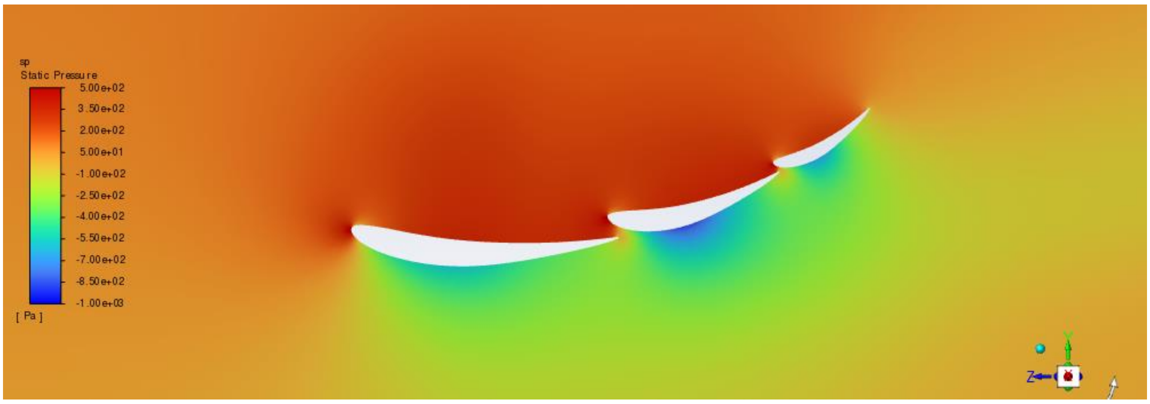

Figure 6-26: Outside Ground Effect Static Pressure Contour

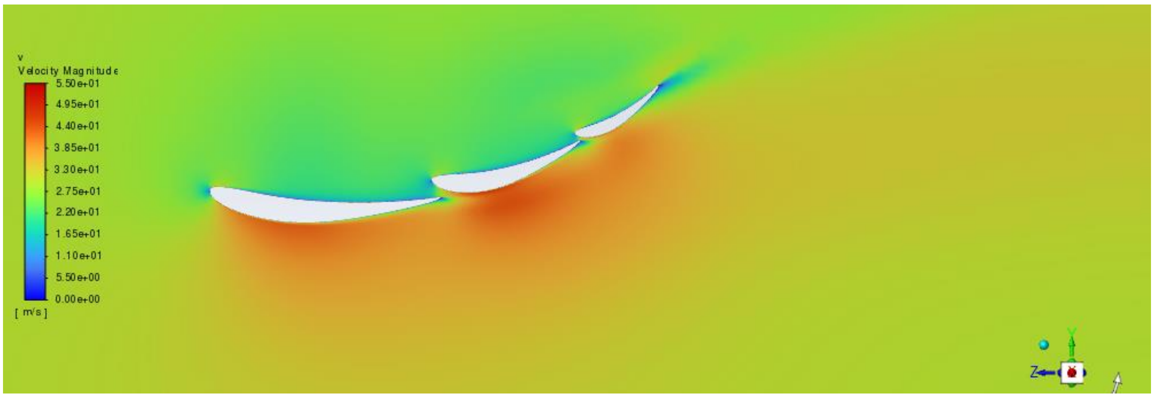

Figure 6-27: Outside Ground Effect Velocity Magnitude Contour

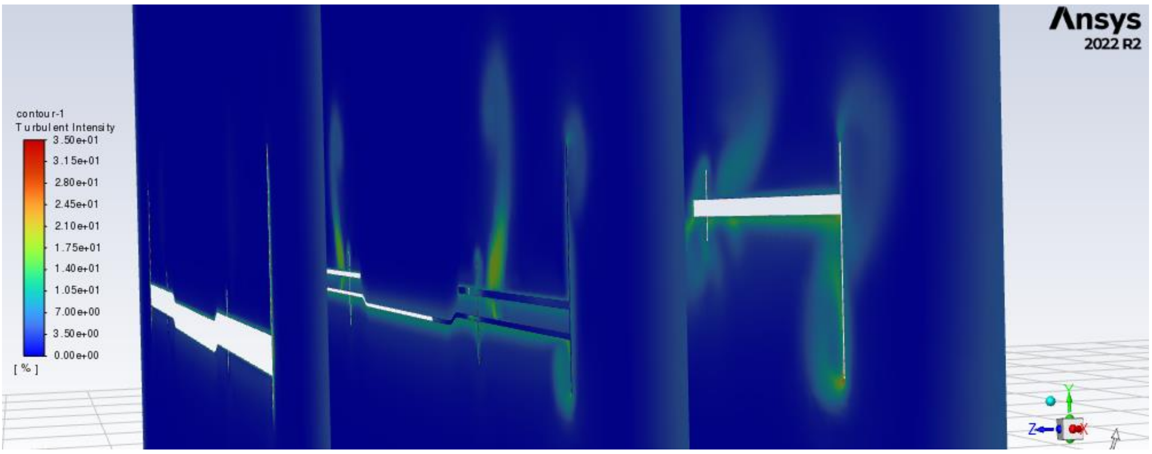

Figure 6-28: Outside Ground Effect Turbulent Intensity Contour

6.5.5. Path-Lines

Analysing the path-lines plotted for turbulent intensity and static pressure along the end plates and below the wing, for the baseline and 8° yaw, it can be shown that even in the baseline high pressure air from outside the wing is being drawn in under the endplates, into the low-pressure region generated below the elements, the mixture of high pressure and low pressure air would then be the cause of the turbulent region apparent in the wake, which is discussed previously.

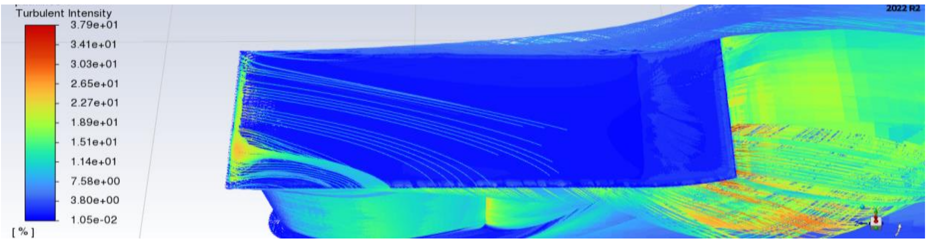

Figure 6-29: Baseline Turbulent Intensity Path-Lines, Endplate

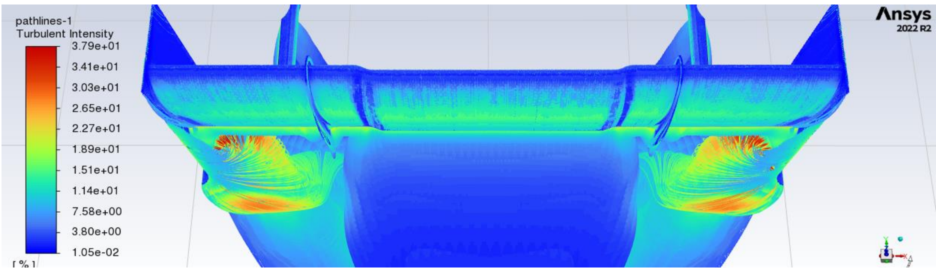

Figure 6-30: Baseline Turbulent Intensity Vortex Regions

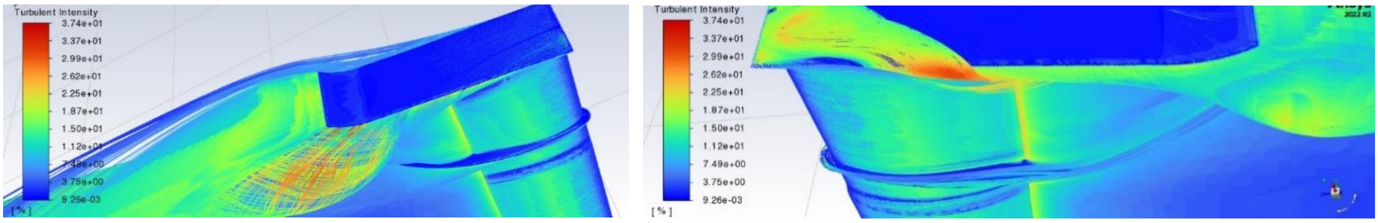

Figure 6-31: 8° Turbulent Intensity Path-Lines, Endplates, Windward & Leeward

Figure-6-32 clearly shows the size and intensity difference between the turbulent regions generated in the wake, on the windward and leeward sides due to the increase in yaw angle. Where the additional airflow against the outside of the windward endplate causes an increase in high pressure air entering the region below the wing, thus increasing the turbulent intensity, while on the leeward side the flow becomes more intense on the inside of the endplate, therefore redirecting flow from the inside of the wing to the outside.

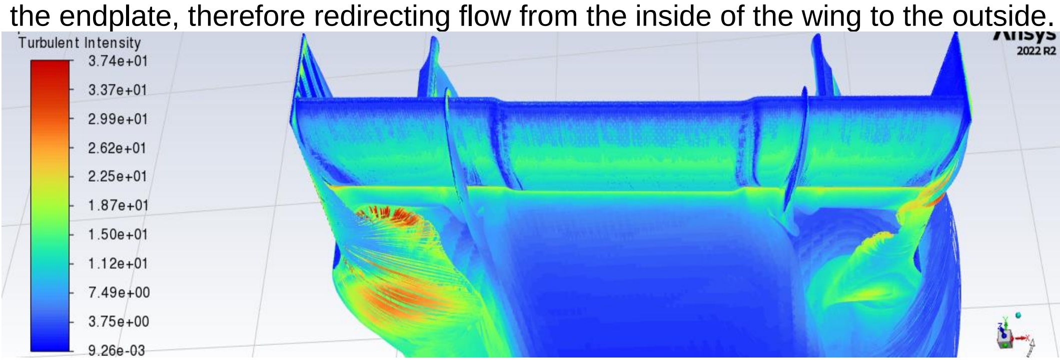

Figure 6-32: 8° Turbulent Intensity Vortex Regions

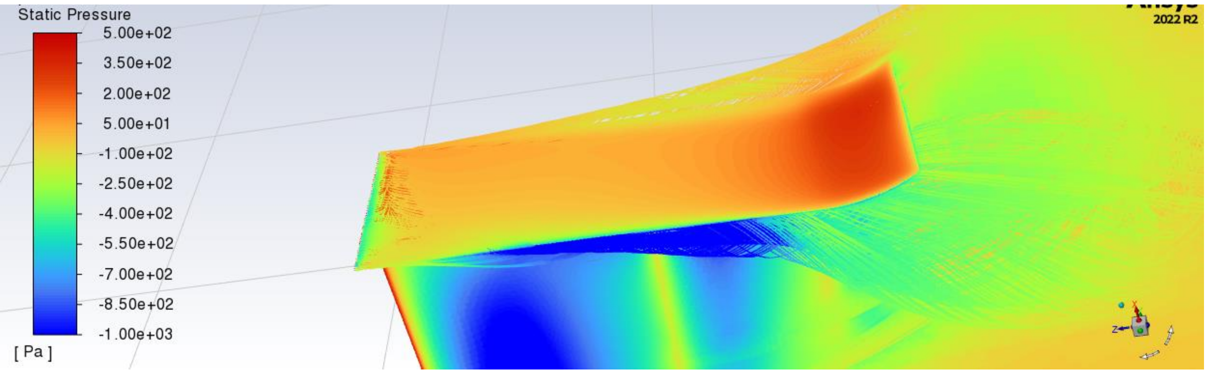

Figure 6-33: Baseline Static Pressure Path-Lines

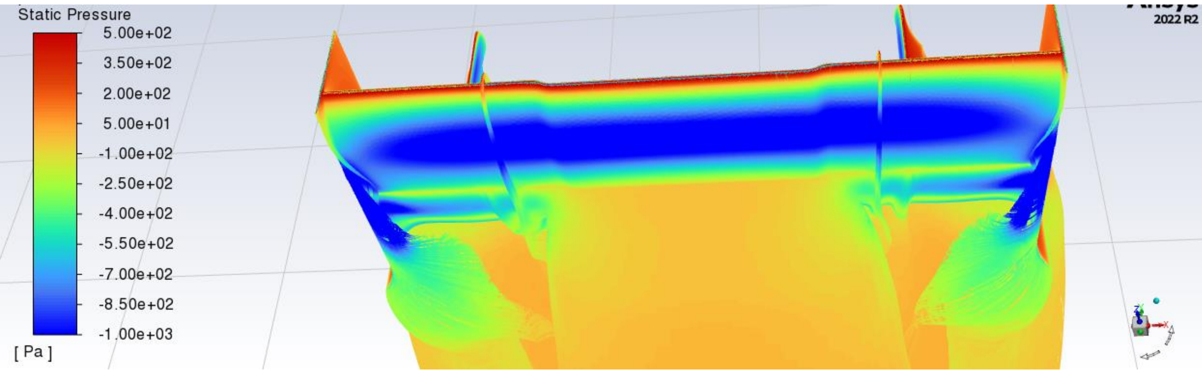

Figure 6-34: Baseline Static Pressure Path-Lines Below the Wing

The windward endplate experiences greater static pressure on the outside due to the increased airflow against it, when compared to the outside of the leeward enplate, thus showing an increase in side force generated on the wing.

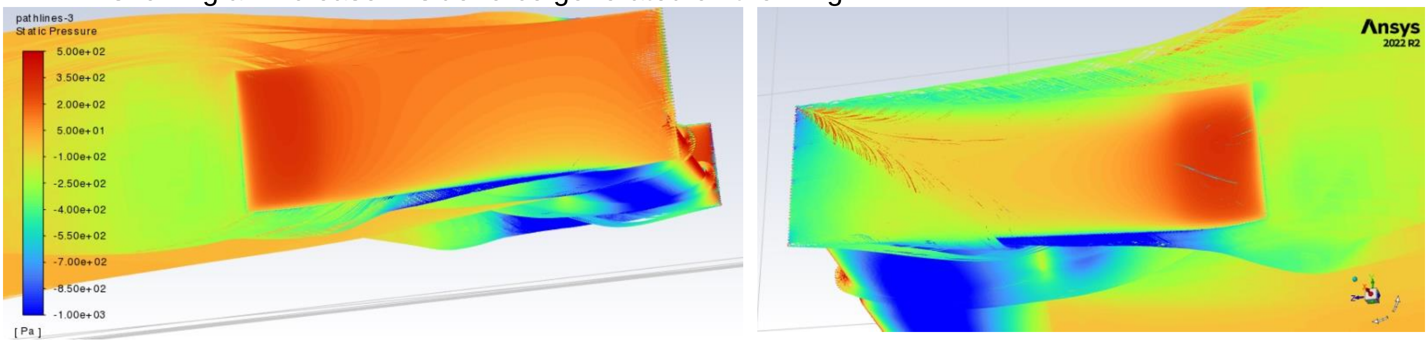

Figure 6-35: 8° Static Pressure Path-Lines, Endplates, Windward & Leeward

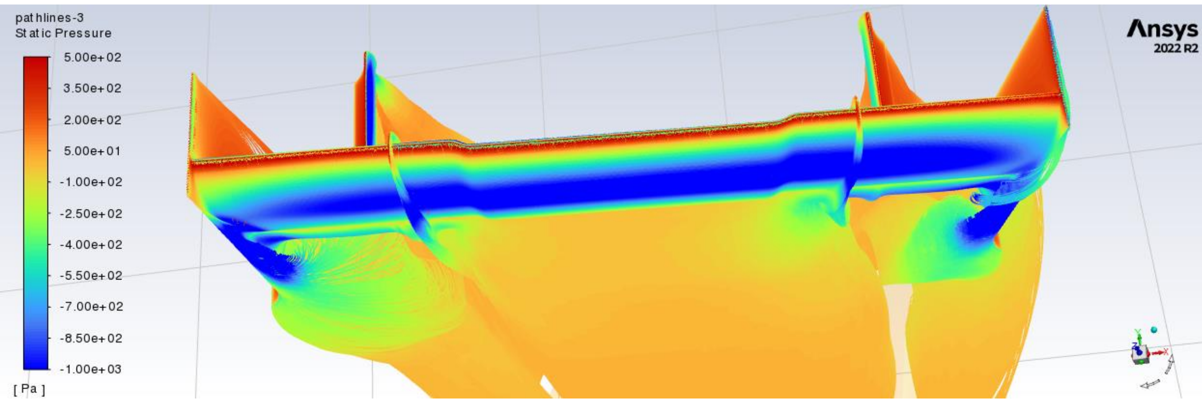

Figure 6-36: 8° Static Pressure Path-Lines Below the Wing

Analysing figure-6-37 shows a clear difference in the wake region generated on the winward and leeward sides of the wing in 8° yaw, where decreased airflow is directed over the element cascade on the windward side.

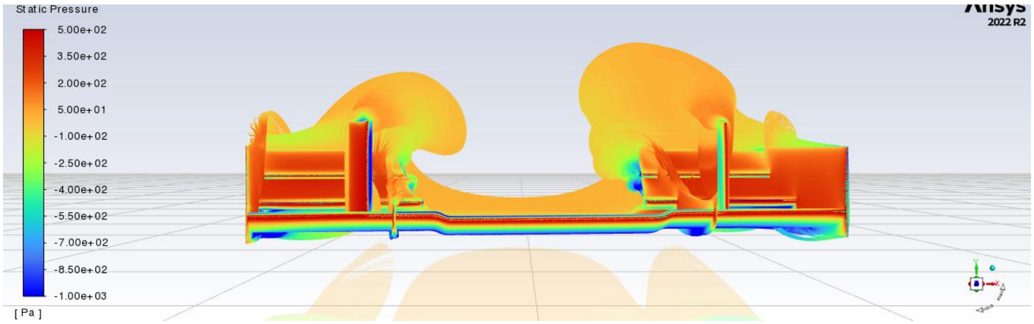

Figure 6-37: 8° Static Pressure Path-Lines Wake Region Difference

The inner side of the endplate on the leeward side experiences a slight increase in static pressure when compared to the inner side of the endplate on the windward side, showing an increase in the side force generated on the wing.

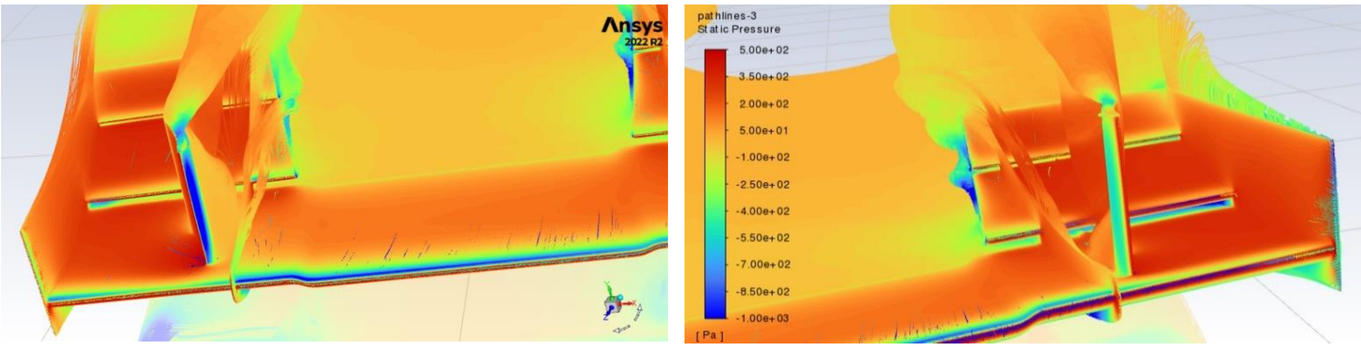

Figure 6-38: 8° Static Pressure Path-Lines Inside Endplates

Plots below show the distribution of static pressure along the surface above and below the wing, where it can be seen the distribution is unevenly distrinuted towards the leeward side due to the additional airflow.

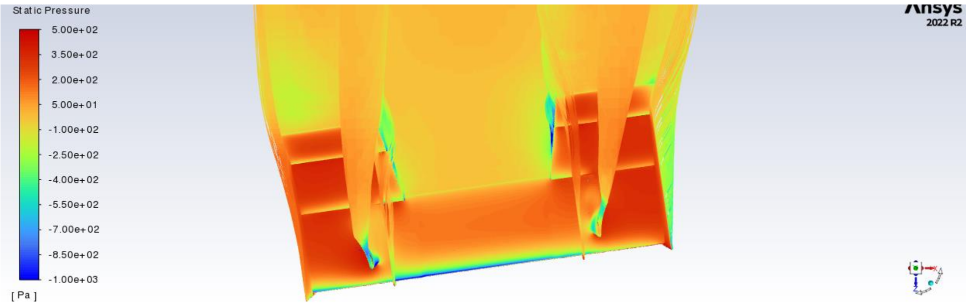

Figure 6-39: 8° Static Pressure Path-Lines Above the Wing

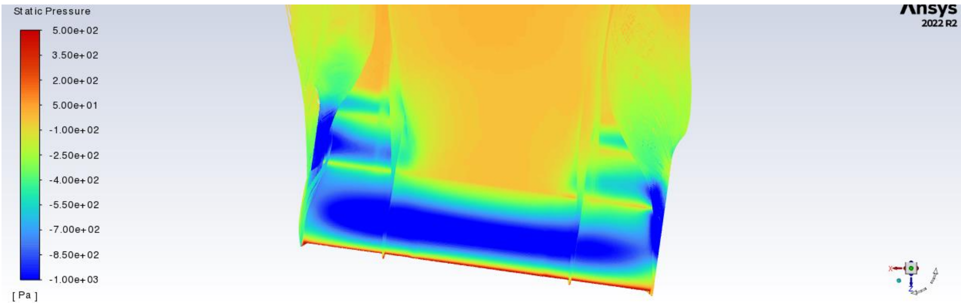

Figure 6-40: 8° Static Pressure Path-Lines Below the Wing

7. Discussion of Results

The results in the previous section demonstrate how the lift and drag forces on the front wing are affected by changing yaw angles, where lift shows a gradually decreasing slope as the yaw angle is increased, while the drag force parallel to the flow direction shows an almost exponential increase with increasing yaw angle, where this drag component is made up of almost linearly decreasing drag and almost linearly increasing side force, where the side force increases at a greater rate than the drag decreases, thus explaining the almost exponentially increasing drag parallel to the flow direction.

The Results from the CFD simulations show strong correlation in terms of the trends produced for lift and drag, when compared to the experimental data.
In the experimental case values produced for lift are shown to be lower than those predicted by CFD, with an almost 18% difference being shown for the realizable k-epsilon model. The k-omega model, however, shows good correlation with values being approximated at less than 1% variation for lift.
While values produced for drag are shown to be higher than those produced by CFD, where the realizable k-epsilon model shows roughly 22% variation in results, while the k-omega model shows roughly 25% variation in result compared to the experimental data.
As the gap between the experimental and CFD data is reasonably consistent across the analysis within less than 2% difference in the gap across each data point in each data set, possible cause for this misalignment in data could be attributed to the setup used within the experimental procedure, where the stand printed onto the model may cause interactions with the flow over the aerofoil, causing early separation, resulting in decreased lift and increased drag, while flow crossing the wing is obstructed in the area where the stand connects to the wing. Interference may also be apparent in terms of ground effect, where the ground proximity is compromised in the stand region.
Other deviations in data could be caused by variations in the geometry due to inaccuracies in 3D printing, where the surface roughness may not be as accurate as that used in the simulations, as well as variations in the geometric metrics. The sensitivity of the strain gauge load cells of the wind tunnel may cause variations in data as well.

The contours and path-lines plotted provide insight into how the flow changes across the wing with variations in yaw angle. Observations made for the wing at 0° yaw show it performs as expected, with high- and low-pressure regions occurring above and below the wing, providing the conditions required for downforce to be generated, as well as the decrease in static pressure due to ground proximity being displayed. However, turbulent regions generated in the wake, beneath the element cascades, caused by the mixing of high- and low-pressure flow around the end plates is a cause for concern, as the turbulent region lowers the effectiveness of the wing due to a reduction in flow velocity below the elements, causing an increase in static pressure, thus reducing the downforce.

Observations made for the wing at 8° yaw show a reduction in the leeward turbulent region, due to airflow against the inside of the endplate, reducing the mixing of high- and low-pressure air, while the windward turbulent region increases in size due to flow against the outside of the endplate, thus increasing the mixing of high- and low-pressure air. The uneven vortex generation is likely to cause increased lift on the leeward side of the wing, where static pressure contours below the wing already show a lower static region towards the leeward side.

The reduced drag is likely caused by decreased airflow over the elements, where airflow is conflicting with the side plates creating an increase in side-force, side-force is not an issue as it aids in cornering by increasing the force towards the centre of rotation. With all observations in mind a recommended focus area for design improvements would be the side plates.

8. Design Improvements

8.1. Geometry

A concept for a design improvement is shown below where a simple footplate has been integrated into the endplate, with the approach taken being to reduce the amount of high-pressure air flowing along the lower edge of the endplate, from mixing with the low-pressure region underneath the wing.

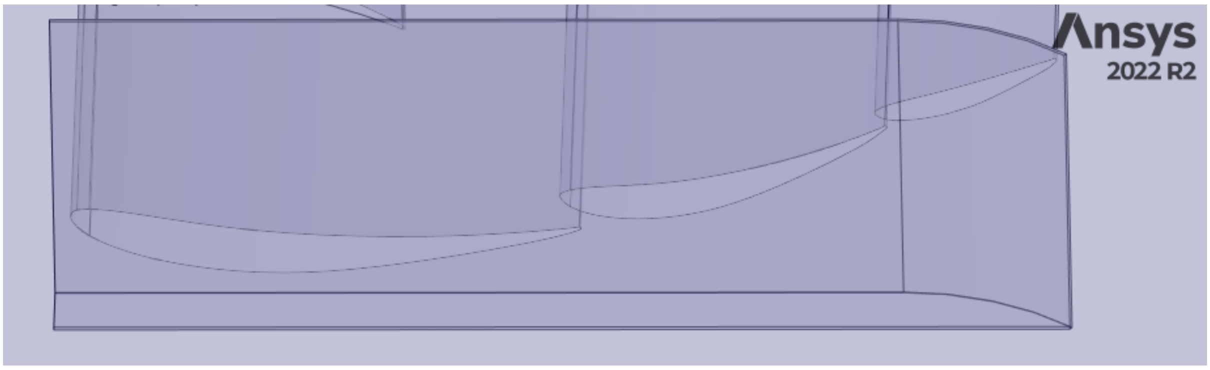

Figure 8-1: Footplate Geometry Improvement

8.2. Results

Results for the footplate geometry compared to the original geometry, show a substantial increase in lift generated at roughly 12% with minimal increase in drag $< 1\%$, showing this design improvement would be effective in improving cornering conditions, by increasing the frictional force preventing the vehicle from going into a slide, with negligible drag increase. The side force shows an increase as well, this is not an issue as this increases the force towards the centre of rotation.

Table 8-1: Footplate Geometry Results

Yaw angle (deg)	0	4	8
Lift (N)	14.562	14.448	14.136
% change from original	13.597	12.937	11.158
Drag (N)	2.6951	2.7128	2.7683
% change from original	0.541	0.634	0.457
Drag Component (N)	2.6951	2.6888	2.6668
% change from original	0.541	0.576	0.131
Side Force Component (N)	0.0088	0.439	0.9152
% change from original		6.549	7.637

Analysing the plots shown below, the increase in lift due to geometry adaptation is shown in figure-8-2, the reduction in lift with increasing yaw angle does appear to be more prominent however, the overall increase in lift outweighs this negative aspect.

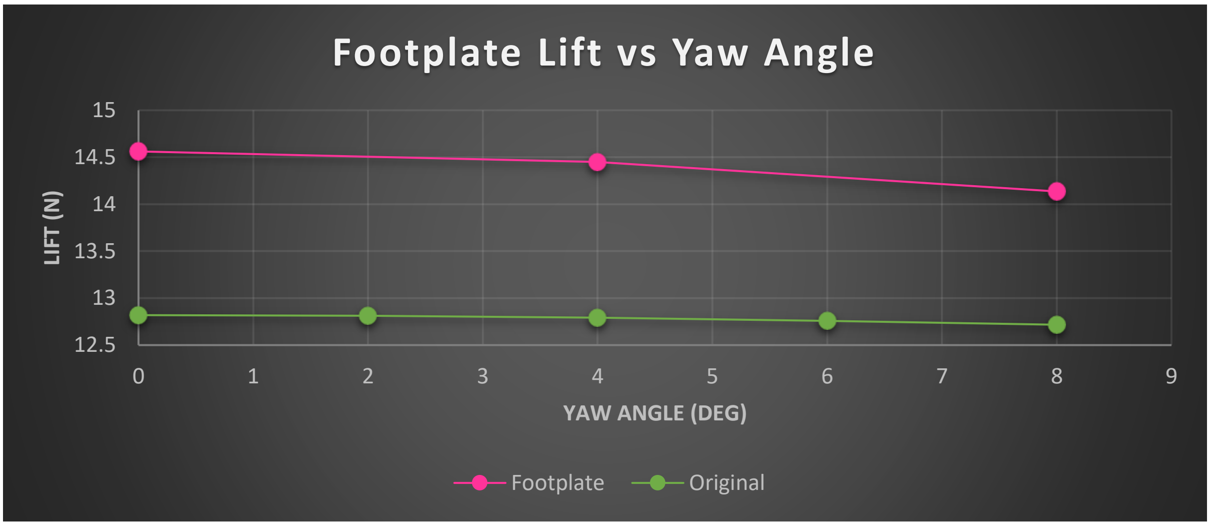

Figure 8-2: Footplate Lift vs Yaw Angle Compared to Original Geometry

Drag vs yaw angle in figure-8-3 shows similarities between the footplate and original geometry where the difference in drag values parallel to the flow direction appears to be almost constant for both geometries.

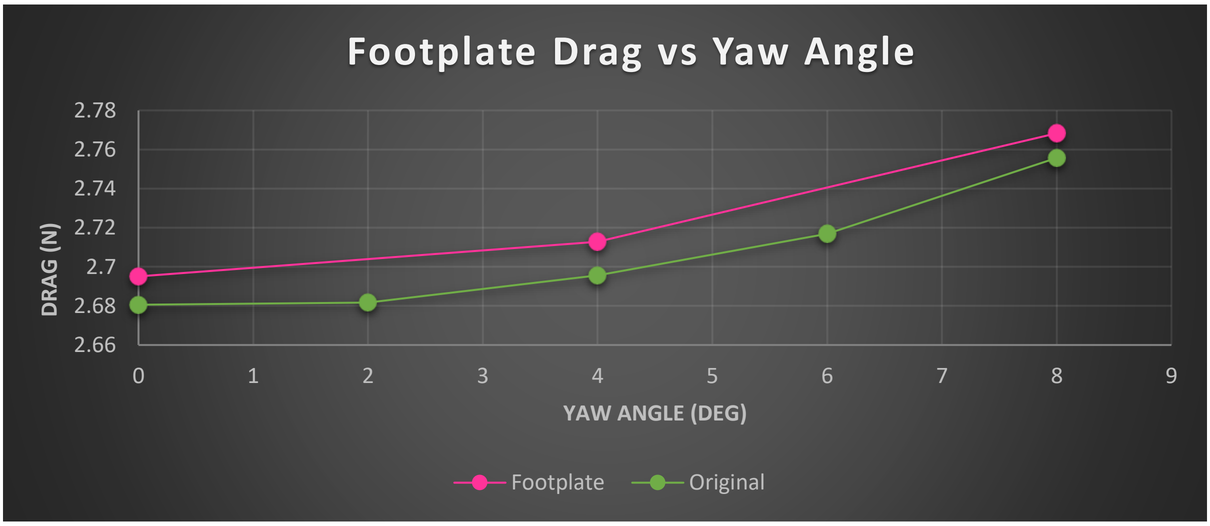

Figure 8-3: Footplate Drag vs Yaw Angle Compared to Original Geometry

The drag relative to the wing vs yaw angle shown in figure-8-4 shows the footplate geometry possesses a much greater reduction in drag towards higher yaw angles compared to the original geometry, with similarities in the slope for low yaw angles.

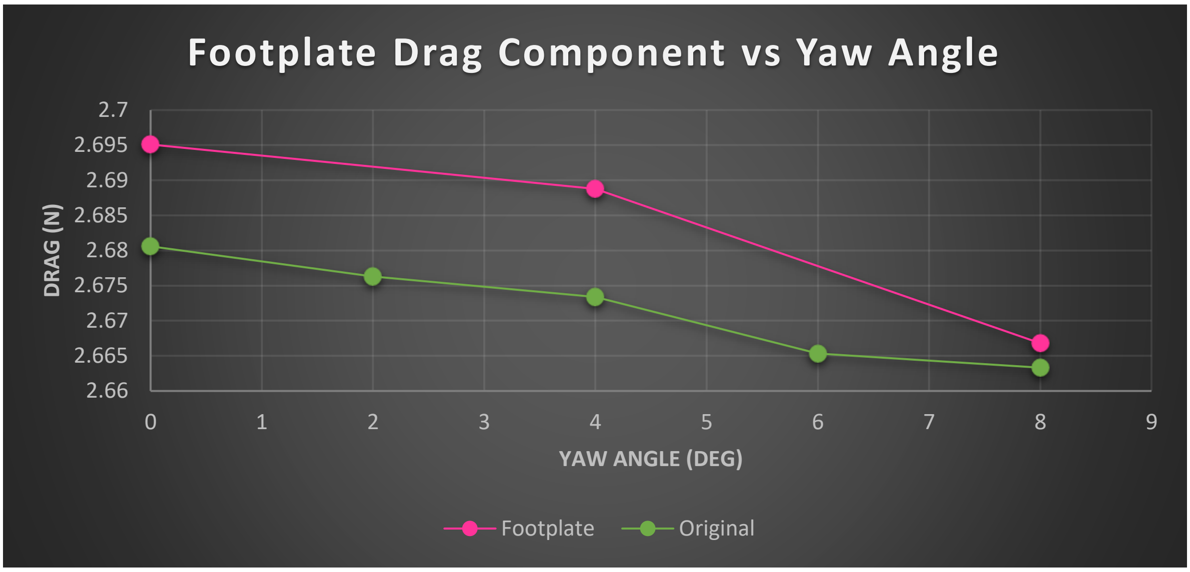

Figure 8-4: Footplate Drag Relative to the Wing vs Yaw Angle Compared to Original Geometry

The side force generated for changing yaw angle, figure-8-5, in both geometries shows minimal change.

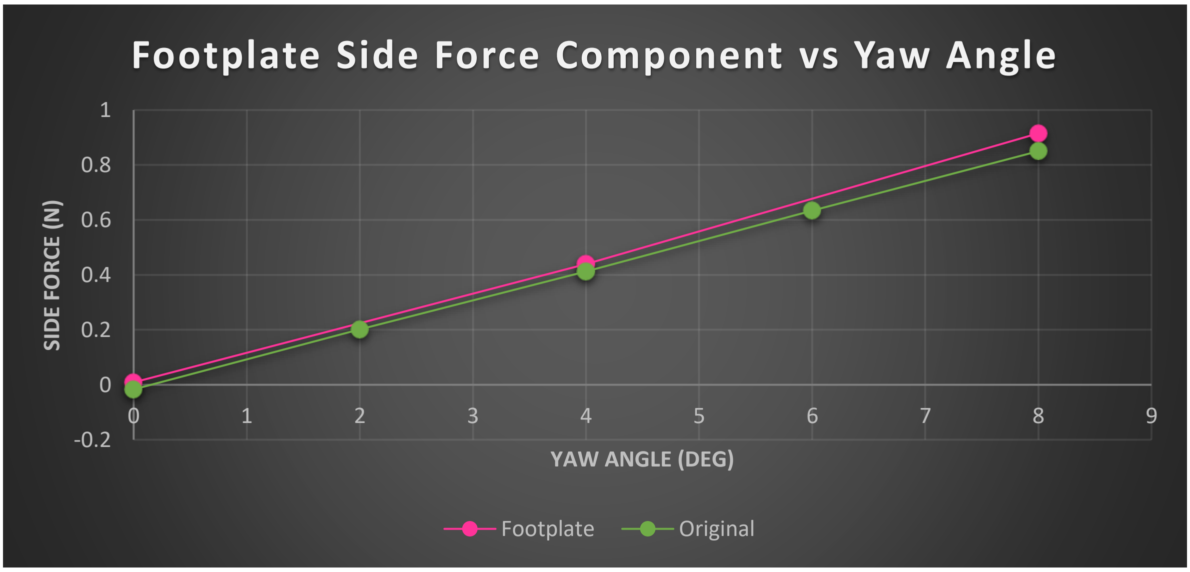

Figure 8-5: Footplate Side Force Component vs Yaw Angle Compared to Original Geometry

8.3. Path-Lines

Path-lines generated for turbulent intensity for the footplate geometry at 0° and 8° yaw are shown below, where it can be seen for the 0° case compared to the original geometry, a delay in the mixture of air from outside and beneath the wing occurs, where high pressure air has to travel further along the footplate, before it reaches a point where it is able to mix with the low pressure region below the wing. A vortex is also generated along the edge of the footplate, blocking a large amount of air from entering the region below the wing,

Turbulent regions generated in the wake appear to be slightly smaller in size however, the main factor is their position, where they appear to occur further into the wake, thus having less of an effect on the element cascades, thus allowing for an increase in downforce generated.

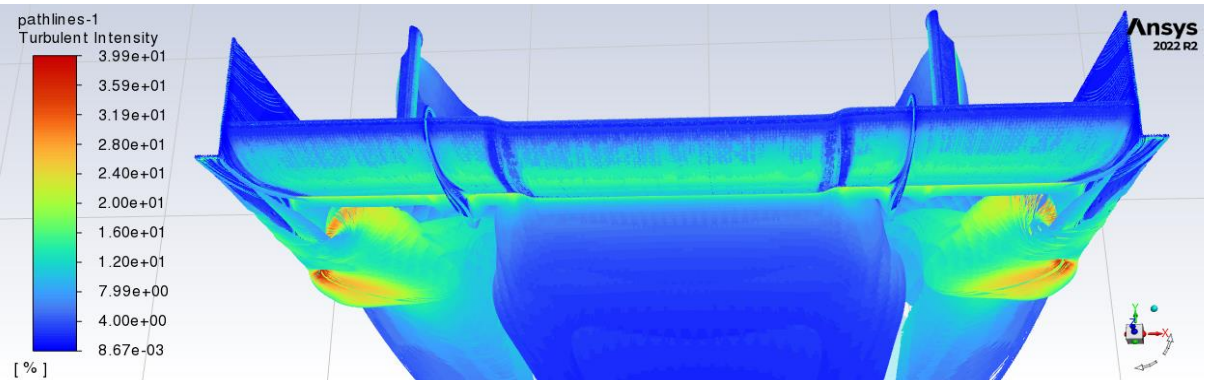

Figure 8-6: Baseline Footplate Turbulent Intensity Path-Lines Vortex Regions

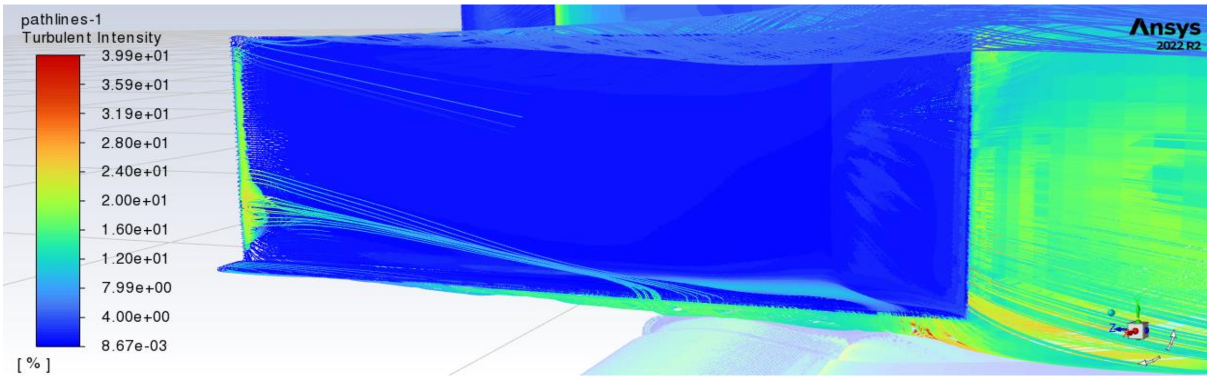

Figure 8-7: Baseline Footplate Turbulent Intensity Path-Lines Endplate

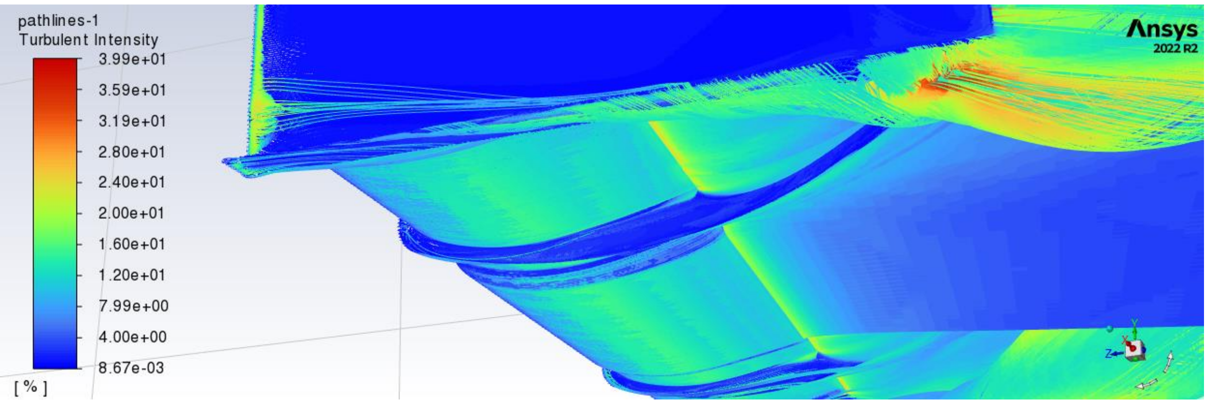

Figure 8-8: Baseline Footplate Turbulent Intensity Path-Lines Vortex Around Footplate

The footplate geometry at 8° yaw shows a similar variation in turbulent region size as shown in the original geometry, however the location of the turbulent region appears to still be positioned further into the wake as discussed with the 0° yaw angle, thus denoting the increase in downforce. The vortex generated around the leeward endplate is however of interest, as it appears to surround the footplate without impeding on the low-pressure region, likely due to its generation further along the endplate, this is likely the cause of the greater drag reduction at higher yaw angles when compared to the original geometry, as induced drag becomes reduced.

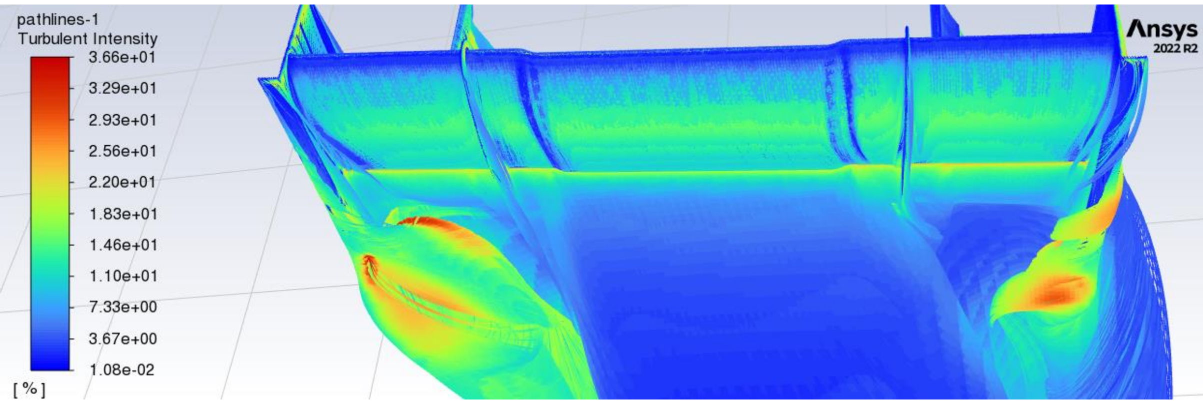

Figure 8-9: 8° Footplate Turbulent Intensity Path-Lines Vortex Regions

Figure-8-10 shows how the high-pressure wake generated on the leeward endplate has to travel further before breaking through to the low-pressure region below the wing.

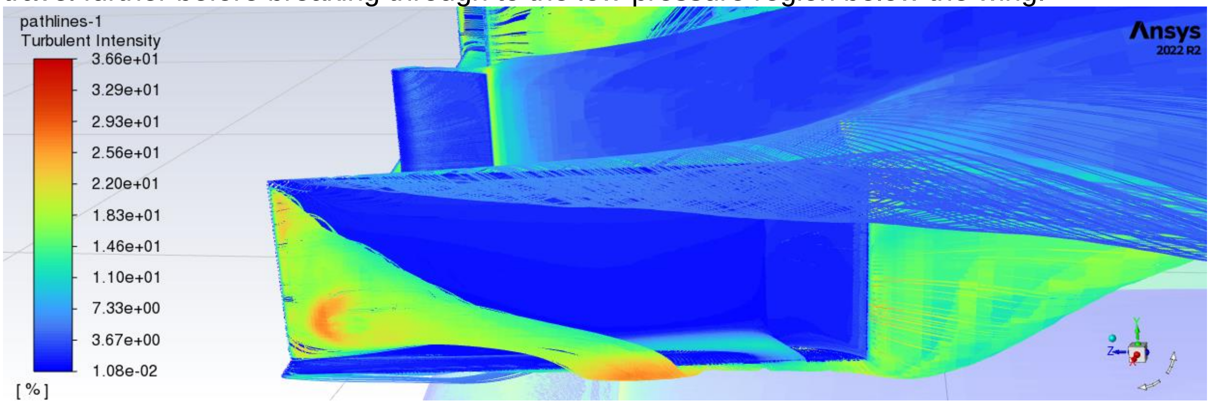

Figure 8-10: 8° Footplate Turbulent Intensity Path-Lines Leeward Endplate

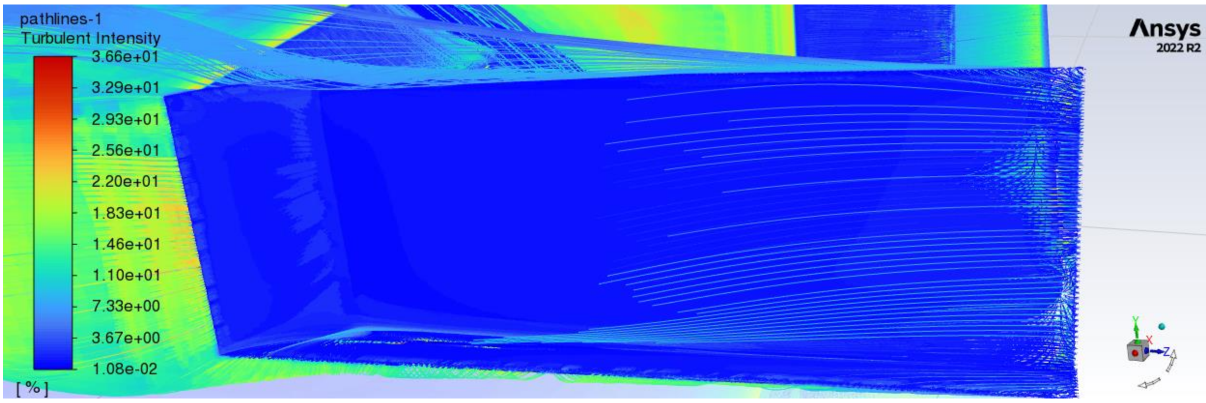

Figure 8-11: 8° Footplate Turbulent Intensity Path-Lines Windward Endplate

9. Conclusion

Within this report a CFD analysis for the change in aerodynamic performance for the SHU Racing front wing at increasing angles of yaw has been performed, where diminishing downforce and drag was observed with increasing yaw, in correlation to that seen in (Roberts et al. 2016). Where a maximum change of 0.8% for lift was observed between the baseline and 8° yaw, and 0.64% change for drag relative to the wing, with the greatest change being observed in the side force.

Flow structures have been analysed showing an uneven distribution in flow, pressure, and vortex generation on the windward and leeward sides of the wing, where the substantial change in vortex size and intensity has been associated with the variation in aerodynamic performance.

Further work has been performed to improve the aerodynamic performance of the front wing, through the implementation of a flat footplate, which has shown a maximum of 13.6% increase in downforce while only increasing drag relative to the wing by a maximum of 0.57%, thus making it a successful design improvement, which is easy to manufacture and implement into the current design.

In addition to the yaw analysis, a comparison between difference in the realizable k-epsilon model and k-omega SST model has been made as well as the effect of ground proximity. Where the realizable k-epsilon model is observed to likely over predict lift and drag, while the k-omega SST model is likely to under predict lift and drag, while both show reasonable accuracy when comparing the predictions made by each model to each other.

Where an experimental analysis was performed as a validation case, the difference in results was larger than expected with the difference for the realizable k-epsilon model ranging from 17.37%-18.86% difference in the case of lift and 21.71%-21.81% for drag, while the k-omega SST model ranges from 0.112%-1.53% for lift and 26.61%-28% for drag. However, with differences being consistent across each point in each analysis, inaccuracies have been attributed towards the experimental setup used.

As the correlation between experimental and CFD results is lower than expected, a suggestion is made for the experimental analysis to be reperformed using an alternative setup, ideally attaching the wing from the upper surface, as well as performing the analysis in a six-axis wind tunnel, allowing for forces relative to the wing to be measured.

With the fundamentals of flow effects being explored throughout this report, there is however room for further analysis, where further research can be made into the sizing of the leeward and windward vortices as well as the effects the footplate has on their position and size. The addition of the footplate is a relatively simple improvement, where further analysis can be made into variation in footplate designs and sizing, as well as their effects on induced drag, vortex generation and wake structure, with the endplates shown to have an influence on the performance of the wing in cornering conditions, a redesign could also be suggested in this area.

10. Personal Reflections

Throughout the process of completing this report, I have greatly progressed my skills in using CFD software in a practical sense, as well as increasing my understanding of the theory and principles behind the simulations, providing an insight into how the programmes operate and produce results. In addition to progressing in the use of CFD, I have obtained a greater understanding of aerodynamics within a motorsport environment, giving me an appreciation of how aerodynamic components are conceptualised and designed for use within the industry. Both of these facets will be advantageous for future progression within SHU Racing.

Apart from practical and design related achievements, completion of this report has also allowed me to develop my management skills, where over the course of the year it has been my own responsibility to manage my time accordingly to reach deadlines, gain an understanding of the topic at hand and generate procedures that allow for the progression and completion of the goals set out.

The greatest challenge experienced during this project was where, the amount of time initially predicted to complete this report was greatly underestimated, where issues in terms of the complexity of CFD, achieving convergence, and gaining access to licensing and adequate computing resources, lead to the dedication of additional time outside of the previously specified commitments, however through adherence and an enthusiasm for the field of study I have persevered in accomplishing the majority of the goals set out.

Overall, this project has been greatly rewarding, providing the opportunity to progress my own skill base, and understanding within an area of my own choosing, which is of great interest to me, thus allowing me to progress as an engineer.

11. References

[1.] Agathangelou, B., & Gascoyne, M. (1998). Aerodynamic considerations of a formula 1 racing car. *Society of automotive engineers (980399)*. From https://doi.org/10.4271/980399

[2.] *ANSYS FLUENT 12.0 Theory Guide.* (2009). From https://www.afs.enea.it/project/neptunius/docs/fluent/html/th/main_pre.htm

[3.] ANSYS, Inc. (2010). ANSYS Meshing User's Guide (Release 13.0) from https://rb.gy/4an0g

[4.] Guerrero, A., Castilla, R., & Eid, G. (2022). A Numerical Aerodynamic Analysis on the Effect of Rear Underbody Diffusers on Road Cars. *Applied Sciences*, *12*(8), 3763. MDPI AG. from http://dx.doi.org/10.3390/app12083763

[5.] Katz, J. (2016). *Automotive Aerodynamics*. John Wiley & Sons, Incorporated. http://ebookcentral.proquest.com/lib/shu/detail.action?docID=7104472

[6.] Martins, D., Correia, J., & Silva, A. (2021). The Influence of Front Wing Pressure Distribution on Wheel Wake Aerodynamics of a F1 Car. *Energies*, *14*(15), 4421. MDPI AG. from http://dx.doi.org/10.3390/en14154421

[7.] Patel, D., Garmory, A., & Passmore, M. (2021). The Effect of Cornering on the Aerodynamics of a Multi-Element Wing in Ground Effect. *Fluids*, *6*(1), Article 1. https://doi.org/10.3390/fluids6010003

[8.] Roberts, L. S., Correia, J., Finnis, M. V., & Knowles, K. (2016). Aerodynamic characteristics of a wing-and-flap configuration in ground effect and yaw. *Proceedings of the Institution of Mechanical Engineers, Part D: Journal of Automobile Engineering*, *230*(6), 841–854. https://doi.org/10.1177/0954407015596274

[9.] TecQuipment. Subsonic Wind Tunnel User Guide. (2015) from https://rb.gy/wvgv1

[10.] Tu, J., Yeoh, G.-H., & Liu, C. (2018). *Computational Fluid Dynamics (Third Edition)* Butterworth-Heinemann. From https://doi.org/10.1016/B978-0-08-101127-0.00003-9

[11.] Read, C., & Viswanathan, H. (2020). An Aerodynamic Assessment of Vehicle-Side Wall Interaction using Numerical Simulations. *International Journal of Automotive and Mechanical Engineering*, *17*(1), Article 1. https://doi.org/10.15282/ijame.17.1.2020.08.0563

[12.] Viswanathan, H. (2021). Aerodynamic performance of several passive vortex generator configurations on an Ahmed body subjected to yaw angles. *Journal of the Brazilian Society of Mechanical Sciences and Engineering*, *43*(3), 131. https://doi.org/10.1007/s40430-021-02850-8

12. Appendices

12.1. Mesh Settings

Sizing Function	Applied to	Sizing Setting	Value
Body of influence (BOI)	BOI	Target mesh size (m)	0.006
Face sizing	Front wing	Target mesh size (m)	0.006
Proximity	Front wing	Local min size (m)	0.0006
		Max size (m)	0.002
		Cells per gap	3
		Scope to	Faces & edges
Curvature	Leading edges	Local min size (m)	0.0003
		Max size (m)	0.002
		Curvature normal angle (deg)	9
Curvature	Trailing edges	Local min size (m)	4.5e-5
		Max size (m)	0.0002
		Curvature normal angle (deg)	9
Curvature	Front wing	Local min size (m)	0.00035
		Max size (m)	0.002
		Curvature normal angle (deg)	9
Surface mesh	Global	Min size (m)	0.002
		Max size (m)	0.02
		Size functions	Curvature & proximity
		Curvature normal angle (deg)	9
		Scope proximity to	Faces & edges

Table 12-1: Surface Mesh Settings

Boundary layer	Applied to	Sizing Setting	Value
Uniform	Front wing	Number of layers	15
		Growth rate	1.23
		First height (m)	1.2e-5

Table 12-2: Inflation Layer Settings

Volume Mesh	Applied to	Sizing Setting	Value
Poly-Hexcore	Front wing	Min cell length (m)	4.5e-5
		Max cell length (m)	0.01152

Table 12-3: Volume Mesh Settings

12.2. IMechE Track Layout and Rules

Dynamics events involving cornering include the Skid-pad event and Autocross event.

Skid-pad track layout.

D4.1.2 The centres of these circles are 18.25m apart. The inner circles are 15.25m in diameter and the outer circles are 21.25m in diameter.

D4.1.3 16 cones are placed around the inside of each inner circle. 13 cones are positioned around the outside of each outer circle, in the pattern shown in the skid-pad layout diagram.

D4.1.5 The driving path is the 3m wide path between the inner and outer circles. The vehicles enter and exit through gates on a 3m wide path that is tangent to the circles where they meet.

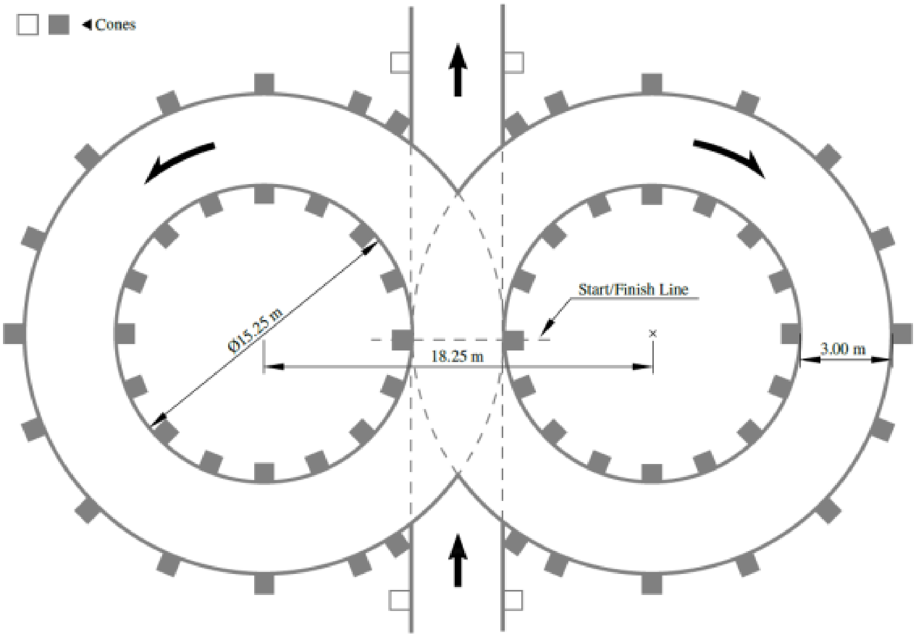

Figure 12-1: IMechE Skid-Pad Layouit

Autocross track layout

D6.1.1 The autocross track layout is a handling track built to the following guidelines:

- Straights: No longer than 80m,
- Constant Turns: up to 50m diameter,
- Hairpin Turns: Minimum of 9m outside diameter (of the turn),
- Slaloms: Cones in a straight line with 7.5m to 12m spacing,
- Miscellaneous: Chicanes, multiple turns, decreasing radius turns, etc. The minimum track width is 3 m.

D6.1.2 The length of the autocross track is less than 1.5km

Restrictions set out by IMechE Formula Student

No parts may come within 75mm of the tyres.

T8.1.2 No power device (e.g., fan) may be used to move or remove air from under the vehicle.

Restrictions for Aerodynamic Devices

T8.2.1 Height restrictions:

• All aerodynamic devices forward of a vertical plane through the rearmost portion of the front face of the driver head restraint support, excluding any padding, set to its most rearward position, must be lower than 500mm from the ground.

• All aerodynamic devices in front of the front axle and extending further outboard than the most inboard point of the front tyre/wheel must be lower than 250mm from the ground.

• All aerodynamic devices rearward of a vertical plane through the rearmost portion of the front face of the driver head restraint support, excluding any padding, set to its most rearward position must be lower than 1.2m from the ground.

T8.2.2 Width restrictions:

• All aerodynamic devices lower than 500mm from the ground and further rearward than the front axle, must not be wider than a vertical plane touching the most outboard point of the front and rear wheel/tyre.

• All aerodynamic devices higher than 500mm from the ground, must not extend outboard of the most inboard point of the rear wheel/tyre.

T8.2.3 Length restrictions:

• All aerodynamic devices must not extend further rearward than 250mm from the rearmost part of the rear tyres.

• All aerodynamic devices must not extend further forward than 700mm from the fronts of the front tyres.

T8.2.4 All restrictions must be fulfilled with the wheels pointing straight and with any suspension setup with or without a driver seated in the vehicle.

T8.3 Minimum Edge Radii of Aerodynamic Devices

T8.3.1 All forward facing edges of aerodynamic devices that could contact a pedestrian must have a minimum radius of 5mm for all horizontal edges and 3mm for vertical edges. T8.4 Aerodynamic Devices Stability and Strength

T8.4.1 Any aerodynamic device must be able to withstand a force of 200N distributed over a minimum surface of 225cm2 and not deflect more than 10mm in the load carrying direction.

T8.4.2 Any aerodynamic device must be able to withstand a force of 50N applied in any direction at any point and not deflect more than 25mm.

12.3. Front Wing Dimensions

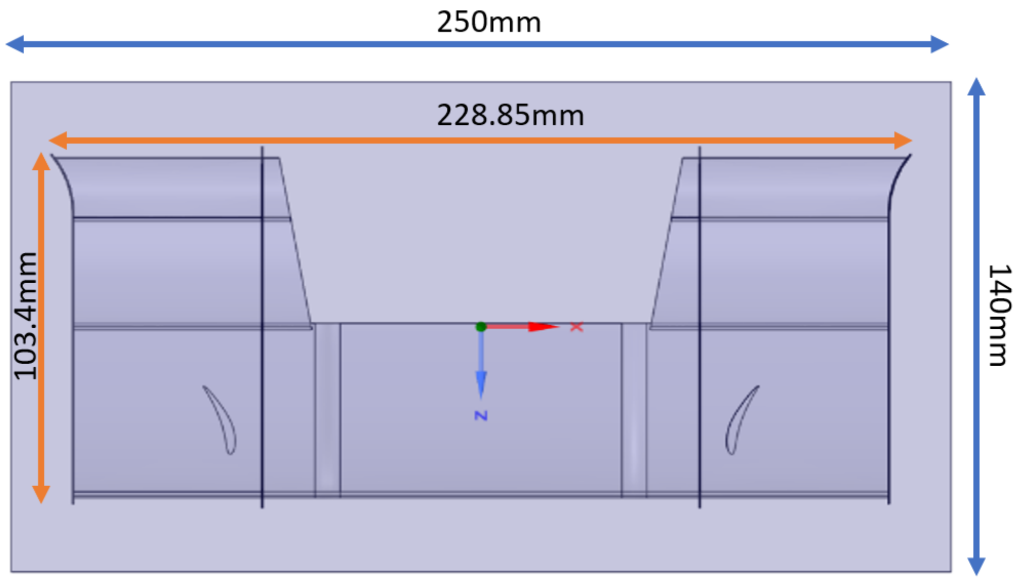

Figure 12-2: Front Wing Dimensions Top

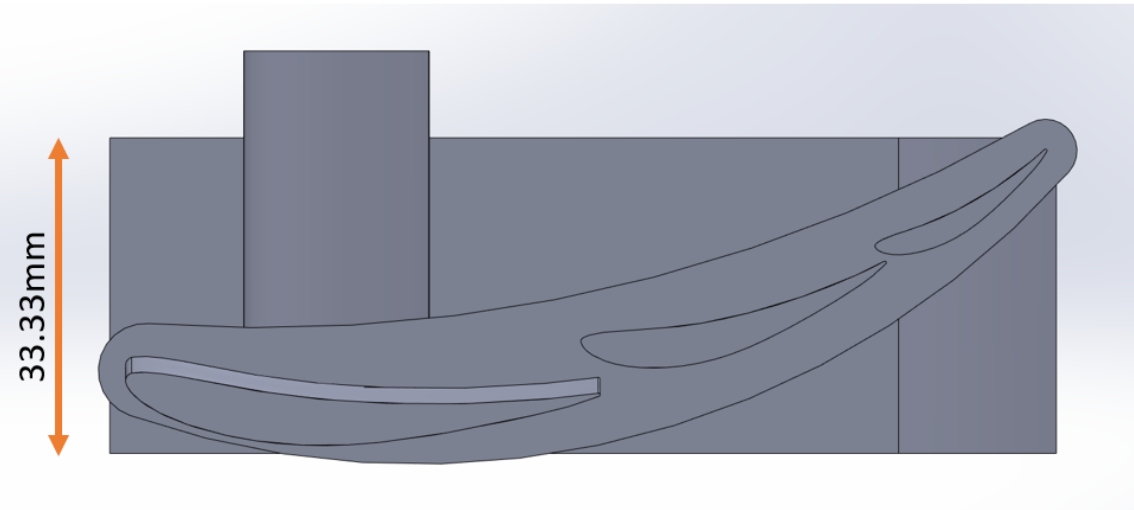

Figure 12-3: Front Wing Dimensions Side